Acoustical Power of Lightning Flashes

Damien Bestard, François Coulouvrat, Thomas Farges, Janusz Mlynarczyk

Acoustical power of lightning flashes

Damien Bestard[1], François Coulouvrat[1], Thomas Farges[2], Janusz Mlynarczyk[3]

[1]Institut Jean Le Rond d'Alembert, Sorbonne Université & CNRS, Paris, France
[2]DAM, DIF, CEA, F-91297 Arpajon, France
[3]Institute of Electronics, AGH University of Science and Technology, Kraków, Poland

Key Points:

- Localisation and quantification of the acoustical power of lightning flashes along the lightning channel in 3D
- Statistics of acoustical power and comparison between different storms and flash polarity
- Comparison between acoustical and electromagnetic parameters

Corresponding author: Damien Bestard, damien.bestard@gmail.com

This article has been accepted for publication and undergone full peer review but has not been through the copyediting, typesetting, pagination and proofreading process, which may lead to differences between this version and the Version of Record. Please cite this article as doi: 10.1029/2023JD038714.

Abstract

Lightning is a ubiquitous source of infrasound. To study lightning flashes, thunder measurement efficiently complements electromagnetic observation. Using acoustical arrays, time delays between sensors inform on the direction of sound arrival, while the difference between emission time and sound arrival provides the source distance. Combining the two allows a geometrical reconstruction of individual lightning flashes, each viewed as a set of sound point sources. The measured sound amplitude can also be back-propagated, compensating for absorption and density stratification. This allows to evaluate the acoustical power of each detected source, and the total power of an individual flash. This methodology is carried out to analyze data from two campaigns in Southern continental France (HyMeX-SOP1, 2012) and in Corsica (EXAEDRE, 2018). Acoustic reconstruction is compared with ground and altitude localizations provided respectively by electromagnetic low frequency range Lightning Location Systems (LLS), and very high frequency range Lightning Mapping Array (LMA). In Corsica, power from reconstructed sources is also forward-propagated towards several isolated microphones, and compared to measured signal, giving an additional validation of the power evaluation. Seventy eight events from the two campaigns are analyzed, including negative and positive cloud-to-ground discharges and intracloud ones. The analysis outlines the method efficiency and the strong variability of lightning as sound sources in terms of both power spatial distribution and overall value. Lastly, the correlation of this later with electrical parameters is investigated, either peak current (provided by LLS) or Charge Moment Change, resulting from broadband Extremely Low Frequency (ELF) measurements.

Plain Language Summary

Lightning is a very powerful event generated by the electric activity inside the clouds. The discharges can occur either inside thunder clouds or connect cloud to ground. The energy generated by a flash is quite difficult to measure or estimate, and its value is still very discussed. Most of the estimations are made by analysing the optical and electric emissions of the flashes, and it appears that it spreads among a wide range of values. As lightning flashes heat up their surrounding air very quickly, they generate a sound that can be detected a few dozen kilometers around. This thunder can be measured by several microphones and processed numerically to reconstruct the 3D shape of the lightning that caused it. The method we use allows to obtain the total power of each detected flash, which seems also very variable. This method also describes the spatial distribution of the power inside each flash. Surprisingly, in most cases, the thunder is not emitted with the same intensity at all by every portions of the lightning. On the contrary, there can be a high variability of the sound power of the different parts of the same lighting flash.

Introduction

Thunder has been investigated since the 1960s, with a view to detect, reconstruct and characterize lightning as an acoustical source. Lightning flashes can be described by numerous variables, among them their total energy per unit length (E_l) which is used in theoretical and numerical models. It can be estimated experimentally by several methods (optics, acoustics or electromagnetics), but its value still remains much discussed. Rakov and Uman (2003) summarize results of previous estimations in their Table 12.1, showing this parameter spreads over four orders of magnitude, from 2 $\mathtt{J.cm}^{-1}$ (Plooster, 1971) to $20,000$ $\mathtt{J.cm}^{-1}$ (M. Uman, 1987).

Acoustical measurements of the total energy of a lightning stroke are mostly based on the model of Few (1969). It describes the lightning channel as a tiny volume of gas around the ionized channel in which this total energy is injected instantaneously (without specifying its origin). This leads to a sharp increase in temperature and pressure that

expands as a strong shock wave into the surrounding air. The strong shock decays into a weak shock, then into an acoustical wave propagating in the atmosphere (Brode, 1959; Few et al., 1967). Taking into account the channel tortuosity leads to assimilate the lightning as a set of point sources regularly distributed along the geometry of the channel (the so-called "string-of-pearl" model), each source being described by this model of strong-to-weak shock transition. In particular, the model provides a relationship between the measurable peak frequency f_m of the thunder power spectrum, and the total injected energy per unit length: $f_m = 0.63 c_0 \sqrt{P_{atm}/E_l}$ where P_{atm} and c_0 are the ambient pressure and sound speed.

The only direct measurement of the total injected energy was achieved for 4-meter long air sparks whose electrical power and energy inputs (about 50 $\mathtt{J.cm^{-1}}$) were controlled (Krider et al., 1968; Dawson et al., 1968). Dawson et al. (1968) obtain empirically the relationship $f_m = c_0 \sqrt{P_{atm}/E_l}$, very similar to the one proposed by Few (1969). Krider et al. (1968) study the same kind of sparks while also quantifying optically their radiated power. Knowing the total energy input, they calculate an optical efficiency of 0.8%. They then use this factor to deduce the total energy per unit length of a natural lightning from an optical observation, finding a value of 2300 $\mathtt{J.cm^{-1}}$. However, this value relies on the questionable assumption of a constant optical efficiency applicable for both air-sparks and natural lightning. Holmes et al. (1971) calculate the acoustical energy of 11 lightning flashes from microphone measurements by temporally integrating the measured power flux, assuming (i) the signal from each temporal window emanates from a single point source, in agreement with Few (1969), and (ii) a homogeneous and non-absorbing atmosphere. This approach is used also by Johnson et al. (2011) on 24 flashes, showing a thunder energy variability of two orders of magnitude. Comparing with the total energy values found by Krider et al. (1968), Holmes *et al.* get an acoustical efficiency of 0.18% (the ratio of total energy converted into acoustic one). Again, this value is controversial (Rakov & Uman, 2003) (see section 11.2.4 p.377, mentioning values up to 20%). Depasse (1994) estimates the total acoustical energy of 12 triggered lightning flashes using their power spectrum measured with a microphone 70 $\mathtt{m}$ away, and Few's relationship between frequency and energy. He gets values between 10 and 1000 $\mathtt{J.cm^{-1}}$. He also shows a good correlation (with a correlation factor of 0.76) between the acoustic energy per unit volume measured at the microphone and the specific energy $E_e = \int I^2(t)dt$, where $I(t)$ is the lightning current. This is the first convincing attempt to correlate acoustic and electric energies of a lightning stroke. A similar correlation (with a correlation factor of 0.978) is obtained recently by Wang et al. (2022) for a single triggered lightning flash leading to 13 successive return strokes acoustically observed at 130 $\mathtt{m}$. Other correlations with peak overpressure or acoustic signal duration on the one side and peak current on the other side, are also reported by these authors. Lacroix et al. (2018) outline a possible correlation between received acoustic energy and charge moment change (CMC, see section 1.1.3) or impulse charge moment change (iCMC) but only for seven intense positive cloud-to-ground discharges (+CGs), which all lead to sprites (Soula et al., 2015) occurring between 40 km and 90 km height. Novoselov et al. (2022) also observe a correlation between vertical displacement of seismic sensors recording thunder and peak current, again for +CGs only.

Few's string-of-pearl model is linked to the tortuosity of the lightning channel. The influence of this one on the acoustic emission has been studied by several authors. For negative cloud-to-ground discharges (-CGs), the tortuosity has been quantified by the observations of Hill (1968); Levine and Gilson (1984); Glassner (2000). This description is used by Ribner and Roy (1982) to propose a numerical model of thunder, assuming a homogeneous distribution of point sources along the tortuous channel, each emitting the same empirically determined weak-shock N-wave. The resulting pressure time waveforms and spectra are compared to observations. Lacroix et al. (2019) extends this approach by using an input temporal waveform resulting from radiation-hydrodynamics simulations in one-dimensional cylindrical geometry (Ripoll, Zinn, Jeffery, & Colestock,

2014; Ripoll, Zinn, Colestock, & Jeffery, 2014), for three different injected energies of 4, 28 and 60 $\mathtt{J.cm^{-1}}$. Seventy-two simulated return stroke channels of randomly generated geometry are compared with 36 return strokes measured at distances between 300 $\mathtt{m}$ and 20 $\mathtt{km}$. A good agreement is found for the injected energies, and the range dependence shows the existence of two regimes of propagation: a cylindrical near-field divergence below $\sim$ 3600 $\mathtt{m}$, and a spherical far-field divergence beyond. Arechiga et al. (2011) use electromagnetic detections of two triggered lightning flashes in the radio frequency (RF) range, provided by a Lightning Mapping Array (LMA), which consists of networked antennas that detect and locate RF pulses produced by ionization events in stepped leaders (Rison et al., 1999). These LMA detections are then considered as identical sources of empirically determined acoustic impulses, the resulting signal being compared to the measured one. Anderson et al. (2014) reconstruct the tortuous geometry of six natural flashes (two CGs and four intracloud ones (ICs)), with a separation of multiple channels. This geometry is identified using LMA RF detections. Then, time backward connections of these detections are performed, and different branching channels are identified. Each channel is discretized as a set of acoustical point sources with the assumption of homogeneous energy distribution. Their relative energy densities are estimated with an optimization method between the simulated and measured acoustical power envelopes. Acoustic energy per unit length is evaluated between 0.02 and 1.6 $\mathtt{J.m^{-1}}$, but only in the narrow $[6-12]$ $\mathtt{Hz}$ frequency range.

Meanwhile, lightning can also be reconstructed from acoustic measurements. The general principle was proposed by (Few, 1970; Few & Teer, 1974; MacGorman et al., 1981). The lightning is decomposed as a set of point sources of thunder according to Huygens principle. The time delay between an array of microphones allows to determine the azimuth and elevation angles of each *coherent* acoustic arrival at the array, while the difference between acoustical time of arrival and electromagnetic time of emission provides the propagation distance between the barycenter of the array and each source. The initial method accounted for heterogeneous atmosphere, using ray tracing to localize the acoustical sources. Nevertheless, good results were found in (Arechiga et al., 2011) for simple propagation (e.g. assuming constant and homogeneous sound velocity with no wind), with a validation by comparison to LMA detections. This was confirmed recently by Gallin et al. (2016), showing statistically that this process with the assumption of a homogeneous and quiescent atmosphere, well matches the LMA reconstruction of the lower and upper charged layers in the clouds for sources at distances less than 10 $\mathtt{km}$. Moreover, it also allows to reconstruct one or several lightning strokes between the cloud and the ground (Lacroix et al., 2018), in good correlation with the ground LLS locations.

According to this literature review, the acoustical energy emitted at the source by lightning has been estimated directly by back-propagation of the overall signal by Holmes et al. (1971) and Johnson et al. (2011). In parallel, acoustical reconstruction methods based on the coherent signal only have been proved to efficiently localize acoustic sources, either within the clouds or within the lightning strokes (Few, 1970; MacGorman et al., 1981; Arechiga et al., 2011; Gallin et al., 2016). However, the combination of reconstruction methods with back-propagation of the measured signal has, to our knowledge, never been used to quantify directly the acoustical energy of a lightning flash and its spatial distribution. In particular, it will allow to compensate for both atmospheric absorption and density stratification, two factors that will be proven here to strongly influence thunder power. This is the purpose of the present work.

First, in section 1 we present the two measurement campaigns that took place in 2012 and 2018 in Southern France, and the corresponding acoustical and electromagnetic data of interest. Then section 2 introduces the methodology for evaluating acoustical power, first by recalling the principle of acoustical reconstruction of individual flashes, and then by back-propagating the thunder signal from the acoustical array to its source, so as to quantify the acoustical power. In the following section 3, several cases of power distri-

butions from both campaigns are discussed, with power distribution analyzed with the help of electromagnetic detections. Section 4 examines the distribution of total acoustical power observed for our overall database of 78 events and quantifies the new elements we take into account (signal coherency, absorption and density stratification) compared to literature. The last section 5 examines the correlation between measured acoustical power and electrical parameters.

1 Experimental setup and available data

Several types of data were used for this study, including both acoustic and electromagnetic measurements of lightning, as well as meteorological data.

1.1 Experimental setup

1.1.1 Acoustical measurements

Acoustic measurements have been carried out by CEA (*Commissariat à l'Energie Atomique et aux Energies Alternatives*) over the last ten years to characterize thunder as part of two campaigns of HyMeX (*HYdrological cycle in the Mediterranean EXperiment*) project (Drobinski et al., 2014). The first one, named SOP1, took place during the fall of 2012 in the Cévennes region (southern continental France, see figure 1) (Ducrocq et al., 2014; Defer et al., 2015). The second one, named EXAEDRE (*EXploiting new Atmospheric Electricity Data for Research and the Environment*) (*EXAEDRE*, 2018) occurred during autumn 2018 in Corsica island. For both, acoustic measurements have been carried out with a mini-array (labeled "`AA`" for *Acoustic Array*) of four microphones (50 `m`-side triangle for SOP1, 30 `m`-side triangle for EXAEDRE), with three microphones at the triangle apex and the fourth one approximately at their barycenter. Microphones were *MCB2006* of bandwidth $[10^{-1} - 10^{4}]$ `Hz` (Lacroix et al., 2018), with a sampling frequency $f_s = 500$ `Hz` for SOP1, $f_s = 250$ `Hz` for EXAEDRE. The data were time-stamped using GPS. For EXAEDRE only, `AA` was complemented by eight isolated microphones (noted $\texttt{SA}_n$, $n = 1$ to 8 for *Standalone Array*) distributed in a radius of 10 `km` around the "`AA`" mini-array. The `SA` microphones were prototypes of *SIS-1* sensor also sampled at $f_s = 250$ `Hz`. Their data-sheet can be found at (*MB3a Analog Infrasound Sensor*, 2022). A permanent meteorological station was located at about 3100 `m` from `AA` at Alistro semaphore. In addition, an anemometer was co-localised with `AA`. The GPS coordinates of the four `AA` microphones, the eight `SA` microphones and Alistro meteorological station are provided in table 1. GPS coordinates of SOP1 sensors can be found in (Gallin et al., 2016). SOP1 and EXAEDRE `AA` and `SA` data are available in databases (Farges, 2023a, 2023b).

1.1.2 Lightning location networks

During SOP1 and EXAEDRE campaigns, lightning information were available thanks to two kinds of electromagnetic detection systems. Firstly, typical Lightning Location Systems (LLS) measure the low frequency (LF, 1 to 350 `kHz`) electromagnetic waves with several stations detecting lightning flashes and giving their time, location (latitude, longitude, error d_R`(in km)`), peak current I_{max}`(kA)`, negative/positive polarity and type of discharge: Cloud-to-Ground (CG) or long IntraCloud (IC). EUCLID (European Cooperation for Lightning Detection) (Schulz et al., 2016) was used during SOP1 campaign, while the French LLS Météorage (Pdeboy, 2015) provided similar LF data during EXAEDRE campaign. Note that tables S1 and S2 in Supporting Information show error values in the order of a kilometer, in agreement with the median value 1.1 `km` of the overall storm (about 100,000 flashes). Secondly, networks of 12 antennas detecting in the very high frequency range (VHF, 60 to 66 `MHz`) were used. They measure the radiation from leaders and intracloud discharges, which occur mostly inside the thundercloud. They pro-

Table 1: Location of EXAEDRE sensors

EXAEDRE	lat [°E]	lon [°N]	altitude [m]
AA	42.2817	9.5198	38
SA 1	42.3287	9.5041	140
SA 2	42.3007	9.5106	182
SA 3	42.2970	9.4891	216
SA 4	42.2858	9.4873	258
SA 5	42.2547	9.4843	155
SA 6	42.2349	9.4517	174
SA 7	42.2497	9.5513	12
SA 8	42.2144	9.5531	2
Alistro	42.2580	9.5400	74

vide the 3D location of these discharges with an accuracy of few meters (Thomas et al., 2004; Coquillat et al., 2019). During SOP1, the HyMeX Lightning Mapping Array (HyLMA) has been purposely deployed (Defer et al., 2015). During EXAEDRE, an equivalent LMA system, named SAETTA (*Suivi de l'Activité Electrique Tridimensionnelle Totale de l'Atmosphère*) was available (Coquillat et al., 2019) .

The WWLLN (*World Wide Lightning Location Network*) provides, since 2003, electromagnetic energy measurements also in the VLF range (Hutchins et al., 2012; Holzworth et al., 2019). VLF radio electromagnetic waves emitted by lightning flashes are recorded by electric field antennas. A few dozens of sensors (11 in 2003, more than 70 since 2013) are sufficient to cover most of the globe with a median location accuracy of about 10 km, and give a detection efficiency of about 10% to 20% for typical flashes - and up to 80% for discharges of peak current above 50 kA. Thus, the WWLLN usually detects one return stroke per flash.

1.1.3 Broadband ELF measurements

In this study we also use the data from a broadband ELF (*Extremely Low Frequency*) measurement system developed at the AGH University of Science and Technology. It is installed at the Hylaty geophysical station in the Bieszczady mountains in Poland (49.19°N, 22.55°E), at 1493 km from SOP1 AA array and 1260 km from EXAEDRE one. Compared to the previous generation equipment at the time of SOP1, the new active magnetic antennas available during EXAEDRE have a broader frequency range (0.02 Hz to 1.1 kHz), which allows to obtain a higher signal-to-noise ratio. As a result, it is possible to measure discharges that were too weak to be identifiable during SOP1. Additionally, the receiver features a Bessel anti-aliasing filter which does not distort the recorded waveform. The current moment waveform and charge moment change (CMC) are reconstructed from the measurements using the method presented by Mlynarczyk et al. (2015). It is an inverse method that enables us to reconstruct the current moment at the source by taking into account the frequency dependent propagation velocity and attenuation of ELF electromagnetic waves based on the model described by Kuak and Mynarczyk (2011). Once the lightning associated with the acoustic measurement has been identified, we reconstruct the current moment waveform and calculate two key parameters: the total CMC and the impulse charge moment change (iCMC). The CMC is an electrical parameter of a lightning flash which is a good characterization of the electric energy inside a flash, as shown by Pasko et al. (1997). The total CMC is obtained by integrating the whole current moment waveform associated with the lightning discharge, including its contin-

uing current. Therefore, it provides the total charge lowered to the ground, multiplied by the lightning channel length. The iCMC characterizes the electric charge transported by the rapidly changing part of the stroke (Berger, 1975). The iCMC is directly proportional to the peak amplitude of the magnetic field component measured by an ELF receiver (Kulak et al., 2012). It can also be obtained by integrating the first two milliseconds of the rapidly changing part of the current moment waveform (Cummer & Lyons, 2004).

To summarize, the available data set is composed of (i) acoustic pressure at each microphone (AA and SA) (Farges, 2023a, 2023b), (ii) Météorage and EUCLID report (date, latitude, longitude, peak current I_{max}, polarity, type CG/IC) (Schulz, 2013), (iii) LMA reconstruction (date, latitude, longitude, altitude, VHF energy) (Rison, 2012; Defer et al., 2021), (iv) ELF measurement and inferred CMC/iCMC, (v) temperature, wind speed and humidity at meteorological station.

1.2 Investigated storms

During the EXAEDRE campaign, at least two thunderstorms passed over or near (within a range of 25 km) the AA station. The first one occurred on September 17th, 2018 with a very dense activity between 11 am and 2 pm, with almost 1.5 CG/hr/km^2. Among all LLS detections, there are 20% of CGs and 80% of ICs. Note that all hours in this paper are given in Coordinated Universal Time (UTC). Local time is UTC+2. Météorage detected 1,880 CG events in a 25 km radius, 845 CG events in a 10 km radius. Then, on October 2nd, 2018 a second storm between 2 pm and 4 pm had a much lower activity: almost 0.2 CG/hr/km^2, the CGs corresponding to 4% of all the detections. Météorage detected 131 CG events in a 25 km radius, 25 CG events only in a 10 km radius. For these two storms, we analyze acoustically 43 flash events according to the following criteria: (i) Météorage detection less than 10km away from AA in order to enable a precise acoustical reconstruction (Gallin et al., 2016); (ii) no masking by another flash whose sound would arrive approximately at the same time (two events must be acoustically separated by at least 20 s); (iii) a sufficient signal (peak pressure above about 0.1 Pa). The no-masking criteria is by far the most constraining one, leading to investigate only 43 events out of a total of 870 CGs within 10 km around AA (a ratio of 4.9%).

We also re-analyze 35 flash events from the SOP1 campaign of the October 22-23 and October 26, 2012 thunderstorms, examples of which have been previously shown by Gallin et al. (2016) and Lacroix et al. (2018). For this campaign, the investigated storms were of very weak activity (8.6×10^{-4} CG/hr/km^2, corresponding to 12.5% of all the detections for the most active part of the 22-23 October thunderstorm, and 5.6×10^{-2} CG/hr/km^2 corresponding to 78% of all the detections for the most active period of the 26 October). This low rate allows to reconstruct flashes acoustically well separated in time, a criteria similar to the second one used for EXAEDRE. Note however that some events up to 30 km from the acoustical array have been reconstructed (Gallin et al., 2016). The characteristics of the 78 studied flash events are reported in Large Table S1 provided in Supporting Information.

2 Methodology

2.1 Reconstruction

In this study, the PMCC algorithm (*Progressive Multichannel Cross Correlation*) is used to detect coherent waves coming from lightning flashes. The time delays between the sensors, used to obtain the arrival angle of the incident wave fronts, are obtained by correlating the signals of the various microphones of AA by frequency narrow-bands on sliding time windows (Cansi, 1995; Cansi & Le Pichon, 2008). The algorithm is used with a logarithmic distribution of the frequency bands, and variable time windows duration

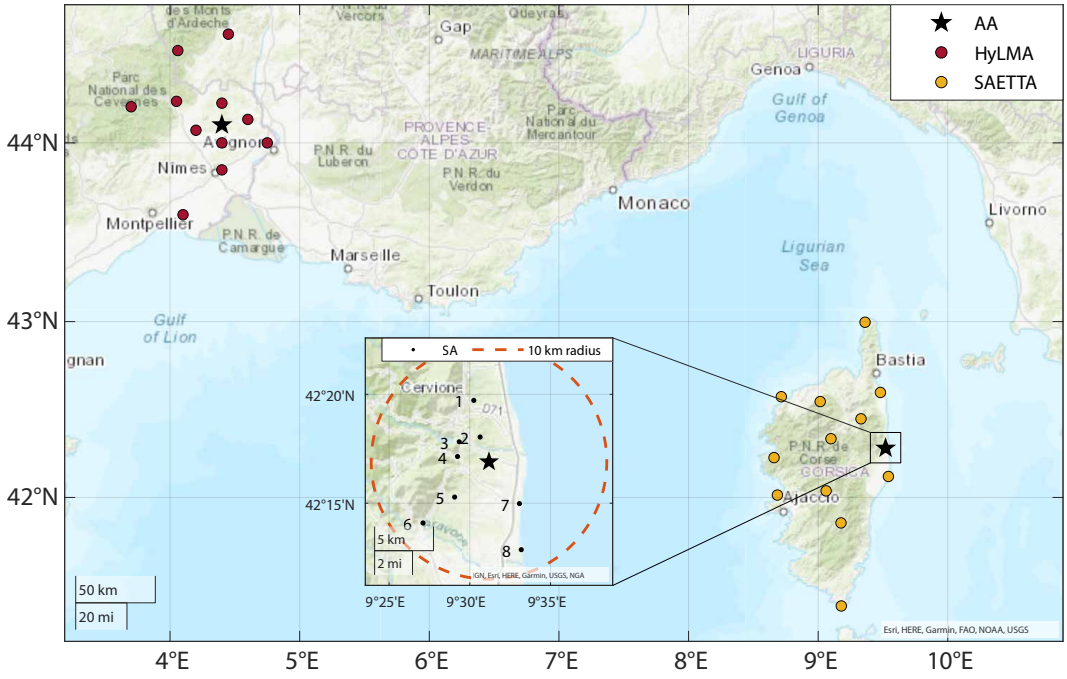

Figure 1: Location of experimental setup for SOP1 and EXAEDRE field campaigns. Dots: VHF electromagnetic antennas of the lightning locating systems for SOP1 (HyMeX-LMA, red) and for EXAEDRE (SAETTA, orange). Black stars: acoustical arrays `AA`. Black dots numbered from 1 to 8: EXAEDRE isolated sensors `SA`.

depending on each frequency band (e.g. 8.2 `s` for $[1 - 1.2]$ `Hz` and 1.0 `s` for $[19.05 - 22.90]$ `Hz` or higher). Time windows have an overlapping rate of 90%. Detailed parameters are provided in Table A1 of Appendix A. A coherent acoustic detection, labeled as a source, is referred by a unique couple $\{F;T\}$ of mean frequency and time intervals of detection at the location of the mini-array `AA`. For each of these detections, PMCC algorithm provides its azimuth angle A (measured clockwise relative to North), its trace velocity V_h, and its RMS (root mean square) pressure $\mathtt{P}^0$. The elevation angle E relative to the horizontal plane is deduced from the ground sound speed c_0 with: $E = cos^{-1}(c_0/V_h)$. The wave propagation time from the source within the flash to the array `AA` is the difference between the measured arrival time T at the array and the time of occurrence of the flash t_{EM}, provided by the LLS: $\Delta t = T - t_{EM}$. Note that t_{EM} is considered as identical for all the sources of the same flash, as the electric discharge in the lightning is virtually instantaneous from an acoustical point of view. In general, for a single flash, the LLS provides several cloud-to-ground detections produced within a short time interval (typically 1 `s`). The reference one chosen for t_{EM} is the first CG or, in case of pure ICs, the most intense one in terms of peak current. As for most studies (Holmes et al., 1971; Arechiga et al., 2011; Gallin et al., 2016; Lacroix et al., 2018), we assume a constant propagation speed equal to the ground sound speed, to calculate the distance r_0 between each source and `AA`: $r_0 = c_0 \times \Delta t$).

For each coherent detected acoustical source found with PMCC algorithm, the Cartesian spatial coordinates are given by the projection

$$\begin{aligned} x &= r_0 \cos E \sin A \\ y &= r_0 \cos E \cos A \\ z &= r_0 \sin E, \end{aligned} \tag{1}$$

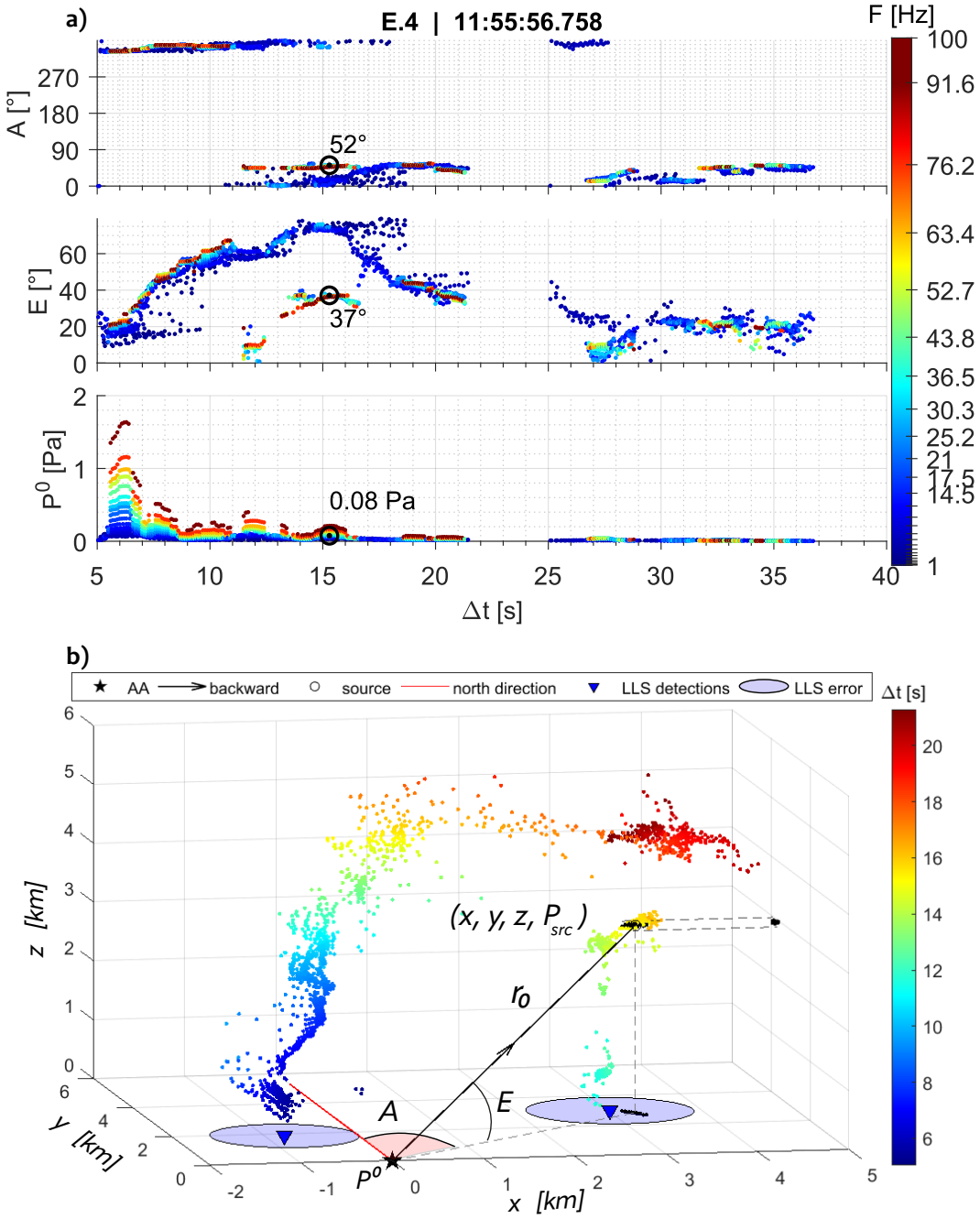

Figure 2: a) from top to bottom: azimuth, elevation and rms pressure detected as coherent by PMCC algorithm as function of detection time relative to emission (horizontal scale) and of frequency (color scale) for event E.4 (2018-09-17 11:55:56:758). b) : corresponding 3D reconstruction of PMCC sources, colored by relative time. Ground triangles : Météorage LF CG detections. Black circle : one particular source point selected to illustrate azimuth (A), elevation (E) and distance r_0 from microphone array (black star). Black points: all PMCC-detected sources emitted at the same time window as this point, and their horizontal and vertical projections. For comparison, blue ground circles are Météorage uncertainty for ground return strokes. Spatial coordinates are given by x: W-E direction, y: S-N direction, z: Altitude.

with x the distance to the array AA in the West-East direction, y in the South-North direction and z the altitude.

An example of the time (horizontal axis) and frequency (color scale) evolution of the three quantities (A, E, P^0) is provided by the figure 2.a for event E.4 (17th Sept. 2018 at 11:55.56.758), with the subsequent reconstruction visible on the figure 2.b. One observes first arrivals from North direction, with an increasing elevation angle. Then about seven seconds later is detected a second set of arrivals, now from North-East and also increasing in altitude with time. The two sets merge about 12 seconds after the first arrivals ($\Delta t = 17$ s), in the north-east direction (52°). The reconstruction shows indeed two vertical return strokes well localized above the LLS Météorage detections, connected by a rather horizontal intracloud layer. In terms of detected rms pressure, the first arrivals, corresponding to the lower part of the first return stroke, are clearly the most intense ones, leading to a peak in the rms pressure followed by several bumps, two emanating from the second return stroke (those observed 12 and 15 seconds after emission). Also noticeable is the fact that the PMCC algorithm, which searches for coherent sources, can detect sources arriving almost at the same time (for instance yellow points in the figure 2.b arriving about 15 safter emission) but from two different zones, for yellow points at the top of the second return stroke and the intracloud region above the first one. From a frequency point of view, lower frequencies (blue points in the figure 2.a) are present all over the acoustical detection period. Higher frequencies (for instance brown points for the highest frequency band) are detected more intermittently, rarely within the intracloud. They are also localized with a higher precision so that the mid and high frequency sources overlap in the (A, E) curves. This is expected for return strokes as sources there are physically localized within the narrow ionized channel. Low frequencies are identified with a lower precision, as their wavelength is larger than the 30 m size of the AA array (corresponding to frequencies around 10 Hz). This error is quantified on the lower figure by projecting (in the horizontal plane and in the vertical direction) all the sources detected during a single, particular time window T. One observes they spread horizontally by around 300 m, and 100 m vertically, an expected order of magnitude corresponding, for a speed of sound around 340 m/s, to the largest time window of 1s used for lowest frequencies. It is noticeable this error is nevertheless significantly much smaller than the one from LLS detections provided by Météorage (horizontal blue circles with a radius of the order of 1 km). To be more general regarding acoustical sources localization near the ground, it turns out that 80% of all sources acoustically reconstructed below 1 km of altitude for all investigated EXAEDRE events, are indeed within the uncertainty margin of Météorage ground detections. This good matching therefore validates the reconstruction process of sources localization used for the evaluation of their power. In the intracloud region, with lower frequency emission, sources are also physically much more scattered, as was already shown by comparison with VHF sources observed there (Arechiga et al., 2011; Lacroix et al., 2018).

2.2 Evaluation of acoustical power

In order to evaluate the acoustical power of a detected point source, we compensate the RMS level detected by PMCC (P^0) at the array for geometrical attenuation, atmospheric density stratification and atmospheric absorption. For this in view, several assumptions must be done. First, the ground is assumed to be perfectly flat and rigid (low-frequency approximation (Attenborough, 1985)), so that the amplitude of the signal measured at the AA network is doubled by ground reflection. Therefore the amplitude P^0 must be divided by two. Second, we assume the source is a point source emitting a spherical wave in a homogeneous atmosphere. This assumption is coherent with the one used for the geometrical reconstruction. Hence, the amplitude of the sound wave decreases geometrically as the inverse of the propagation distance, r_0, between the reconstructed source and the array (AA). Therefore, in the back-propagating phase, the amplitude has to be multiplied by r_0. During its propagation, the wave undergoes phys-

ical absorption due mostly to molecular vibrational relaxation of diatomic nitrogen and oxygen molecules in the air. This process is dependent on the atmosphere humidity and temperature, and on the wave frequency (*ISO 9613-1*, 2003). Both Bass (1980) and later Lacroix et al. (2019) outline the importance of absorption for thunder propagation. Because of this absorption, the wave amplitude is exponentially decreasing with distance, and this has also to be compensated for back-propagation. At last, between the source and the ground and according to ray theory (Blokhintzev, 1946), pressure amplitude is also reduced by the ratio $\sqrt{\frac{\rho_0(z)}{\rho_0(0)}}$ where $\rho_0(z)$ is the density at altitude z of the source in the standard atmosphere (ICAO, 1993). This exponential decay of density with altitude, which is quite stable regarding the meteorological situation, cannot be neglected for high altitude sources. For back-propagation, the inverse ratio $\sqrt{\frac{\rho_0(0)}{\rho_0(z)}}$ has therefore to be applied. This leads to the source pressure level $\mathtt{P}_{src}$ of each detection

$$\mathtt{P}_{src} = \frac{1}{2}\frac{r_0}{r_{ref}}\sqrt{\frac{\rho_0(0)}{\rho_0(z)}}\exp(\alpha r_0) \times \mathtt{P}^0. \tag{2}$$

Coefficient α is the absorption coefficient ($neper/m$) according to the standard ISO-9613-1. It has been computed with the temperature corresponding to the selected speed of sound, and with a 70% humidity, a value measured at the beginning of each specific storm of EXAEDRE and also selected for SOP1 as done by Lacroix et al. (2018). The humidity tends obviously to increase during the storm, but simulations with a 95% humidity level lead to almost unchanged values. The frequency used for the computation of α is approximated as the window mean frequency F attributed by PMCC to the source. The quantity r_{ref} is introduced so that $\mathtt{P}_{src}$ is homogeneous to a pressure and is chosen equal to 1 `m`. All these assumptions amounts to consider that the detected source is emitted at the instant t_{EM} (identical for all acoustical sources of a same flash) with an acoustical signal of RMS level P_{src} at $r = r_{ref}$ in the considered frequency band.

The black arrow of figure 2.b (3D reconstruction) illustrates this back-propagation for one reconstructed point source of event E.4. The computation of $\mathtt{P}_{src}$ from each PMCC detection is then used to determine the acoustical power of each source defined by:

$$\mathcal{P} = \frac{2\pi r_{ref}^2 \mathtt{P}_{src}^2}{Z_0(z)} = \frac{\pi r_0^2}{2Z_0(0)}\left(\frac{\rho_0(0)}{\rho_0(z)}\right)^2 \left(\mathtt{P}^0\right)^2 \exp(2\alpha r_0), \tag{3}$$

where $Z_0(z) = \rho_0(z)c_0$ is the acoustical impedance of air at the altitude of the source. The value of power is independent of r_{ref} as $\mathtt{P}_{src}$ is inversely proportional to r_{ref} (equation 2). Equation 3 is valid for a point source in a non-absorbing medium, an assumption well satisfied here because absorption is negligible over the distance r_{ref}. Regarding the density stratification, equation 3 outlines its importance. For instance at altitude 10 `km`, the density is about one third its ground value, and therefore leads to an increase of acoustical power of a ratio nine. On the contrary, sound velocity varies only less than 15% and is therefore chosen constant, in agreement with the propagation assumptions. We can also estimate the associated energy of each source in the corresponding frequency band F and observation time window T as:

$$\mathcal{E} = \frac{\mathcal{P}}{2\pi F}. \tag{4}$$

To calculate the total power and energy of a flash, we simply sum the value of all detections

$$\mathcal{P}_{tot} = \sum_{flash} \mathcal{P}, \tag{5}$$

$$\mathcal{E}_{tot} = \sum_{flash} \mathcal{E}. \tag{6}$$

3 Spatial distribution of acoustical power

3.1 Application on two typical EXAEDRE events

Fourty-three EXAEDRE events from both September 17th and October 2nd thunderstorms were reconstructed including positive and negative Cloud to Ground (CG) strokes, as well as Intracloud (IC) discharges. For September 17th, 2018, we chose c_0 equal to 350 m/s. This one corresponds to the average value of V_h equal to 349.4 m/s, measured for ambient noise in the absence of thunder, thus corresponding to the speed of sound of remote noise sources arriving with an almost zero degree elevation angle. It is also in agreement with the ground temperature 28.6°C measured at the beginning of the storm. This one decayed slowly during the storm down to 20°C. For October 2nd, 2018, we chose c_0 equal to 340 m/s for similar reasons. We show here two lightning flash reconstructions as examples: event E.4, a -CG on September 17, 2018 at 11:55:56.757 UTC (figure 3.a) ; and event E.34, a +IC from the same day at 13:42:24.586 UTC (figure 3.b). Event E.4 is the one already chosen for figure 2, but with a longer time interval analyzed including a third, more distant, return stroke. These two examples have been selected because they are of different types (a -CG versus a +IC) while having a similar total power P_{tot} of about 3 MW, close to the mean value of all events we analyze.

Figure 3.a shows the reconstruction for event E.4 with sources now colored by their acoustical power. Météorage identifies three -CG strokes located along a S-W to N-E axis and with peak current decreasing in time (see table S1 in Supporting Information). As already discussed, the first two are clearly reconstructed by acoustics with sound sources all along the return stroke channels from the ground up to the two charged layers inside the thundercloud. These ones are also well identified acoustically (see the S-N vertical projection in figure 3.a), at altitudes about 3 and 5 km for respectively the negatively and positively charged layers. However, their south-westward extension is not reconstructed by acoustics as it goes vertically over the AA array. The acoustical reconstruction of the third -CG stroke is more diffuse, and seems to be inclined in the S-E to N-W direction from the top charged layer to the ground, with a W-E extension of about 3 km and a S-N one of about 2 km. The corresponding Météorage ground detection appears located under its upper part rather than at its ground impact. In between, (see the SAETTA points located above the 6 km in SN/altitude projection, each charged layer shows a continuous though less dense SAETTA reconstruction, but with almost no acoustical detection. The two IC Météorage detections correspond to the position of the upper part of the main return stroke and to the area of most dense SAETTA observations. The 3D localization of acoustical power outlines that the most energetic sound sources are located within the three return strokes. The source with maximum power reaches 61.8 kW (localized at 993 m altitude) for the first stroke, 12.8 kW (at 687 m alt.) for the second one, and 0.8 kW (at 1717 m alt.) for the third one. The main peak of the RMS pressure (see figure 2.a) is due to the lower part of the first CG (see the dark blue sources corresponding to the first detections in figure 2.b. Then, successively, several secondary peaks are detected, corresponding respectively (in their order of arrival) to the middle (around 2 km altitude) then the top (around 3.5 km altitude) of the first CG (see figure 2.a and also figure S1 in Supporting Information for another presentation). The same sequence of three peaks is observed emanating from the second CG at about the same altitudes. The last peak emanates from the bottom of the last CG. In between we observe two small peaks due to the lowest intracloud charged layer. However, all intracloud sources (those with altitude above 4 km) have an acoustical power below 2.7 kW (peak value corresponding to the top of the second return stroke at 4.6 km in altitude).

For event E.34 reconstructed in figure 3.b, Météorage detected 6 +ICs (see table S2 in Supporting Information), all located in a narrow zone right under a vertical intracloud discharge connecting the lower and the upper charged layers. These two layers obviously include both VHF and acoustical sources. The median altitudes of each layer is detected at 6600 m and 11080 m by SAETTA, 7160 m and 11840 m by acoustics, with

similar layer thicknesses of the order of one kilometer. Assuming the EM and acoustics layers should be roughly at the same altitude heights, this observed shift can be explained by the simplifying assumption of a constant speed of sound, which tends to overestimate the propagation distance. Taking into account a standard, mild, vertical temperature profile (-6.5 `K/km`) tends to reduce this difference. Sharper gradients occurring in case of storm, where cold air in altitude contrasts with hotter air near the ground, are expected to further reduce this difference. This uncertainty has however moderate impact on the evaluation of power. The most sensitive factor is the density ratio at power 2, which increases by 20% for an over-evaluation of one kilometer of altitude. Adding a 10% uncertainty in terms of distance, this provides an overall estimation of the precision of the power calculation for the highest sources of about 30%, lower ones being more precise. The most intense sound sources are localized within the top positively charged layer, as could be expected for a +IC events (maximal power 17.8 `kW` at $Z = 12.34$ `km`). They correspond to the second peak detected at the station `AA` (see figure S2 in Supporting Information) with the highest amplitude (0.08 `Pa`). The first peak of lower acoustical detected amplitude (0.06 `Pa`) comes from the low negatively charged layer and arrives earlier because of its lower altitude (see figure 3.b). This layer has a source of maximal power 3.2 `kW` at altitude $Z = 8.62$ `km`. This peak is well located above Météorage main detection and also matches with the positions of SAETTA detections connecting the two charged layer. On the contrary, the main acoustical peak is located closer to `AA`. Note that if we assume a relatively intense acoustic source, located at the vertical of Météorage detection and at about 11 `km` of altitude (mean SAETTA altitude of the upper charged layer), this virtual acoustical source would arrive at about the same time as the actually measured main peak.

For these two cases E.4 and E.34, Appendix B presents the rms pressure envelope of coherent signals first back-propagated from the array `AA` to their PMCC-detected sources, and then forward-propagated from these sources to the various isolated sensors `SA`. The reasonable agreement with the signal measured there, both in terms of amplitude and shapes, further confirms the validity of our approach.

The total acoustical power of these two events is respectively 3.0 `MW` and 2.9 `MW`. Without compensating for absorption and stratification, these powers would have been equal respectively to 2.0 `MW` and 264 `kW`. For the CG event (E.4), whose main sources are located in the return strokes, the influence of absorption and stratification over the total power value is significant (an augmentation of a factor 1.5). For the IC event (E.34), it dramatically increases the power of a factor almost 11 due to the high altitude of the main sources. The influence of considering the absorption and stratification is quantified in section 4.2 for all the measured events.

3.2 Other types of flashes

The method of sound flash power evaluation using 3D localisation of sources presented in details for two examples has been applied to the 78 flash events of our database. In the present section, we first present 5 additional cases, in order to emphasize the variability of either the structure of the acoustical power distribution, its total value, and to introduce the different categories of events we dispose of. We respectively present a powerful +CG (52.4 `MW`) that gave rise to a sprite event (S.8, 2012-10-22), a moderate +IC event (0.7 `MW`), also from SOP1 campaign but from another storm (S.29, 2012-10-26), a moderate (1 `MW`) -CG from EXAEDRE (E.2, 2018-09-17) showing a power distribution very different from E.4, a +CG event (E.12) on the same day with a low acoustical power of 0.2 `MW`, and finally a -CG event of moderate power 1.1 `MW` from the last day of EXAEDRE campaign (E.35, 2018-10-02) with a very low density of lightning. Figure 4 shows the projection in the W-E vertical plane for these 5 events. Their 3D projections are shown in Figures S6 to S10 in Supporting Information. The forward-propagation

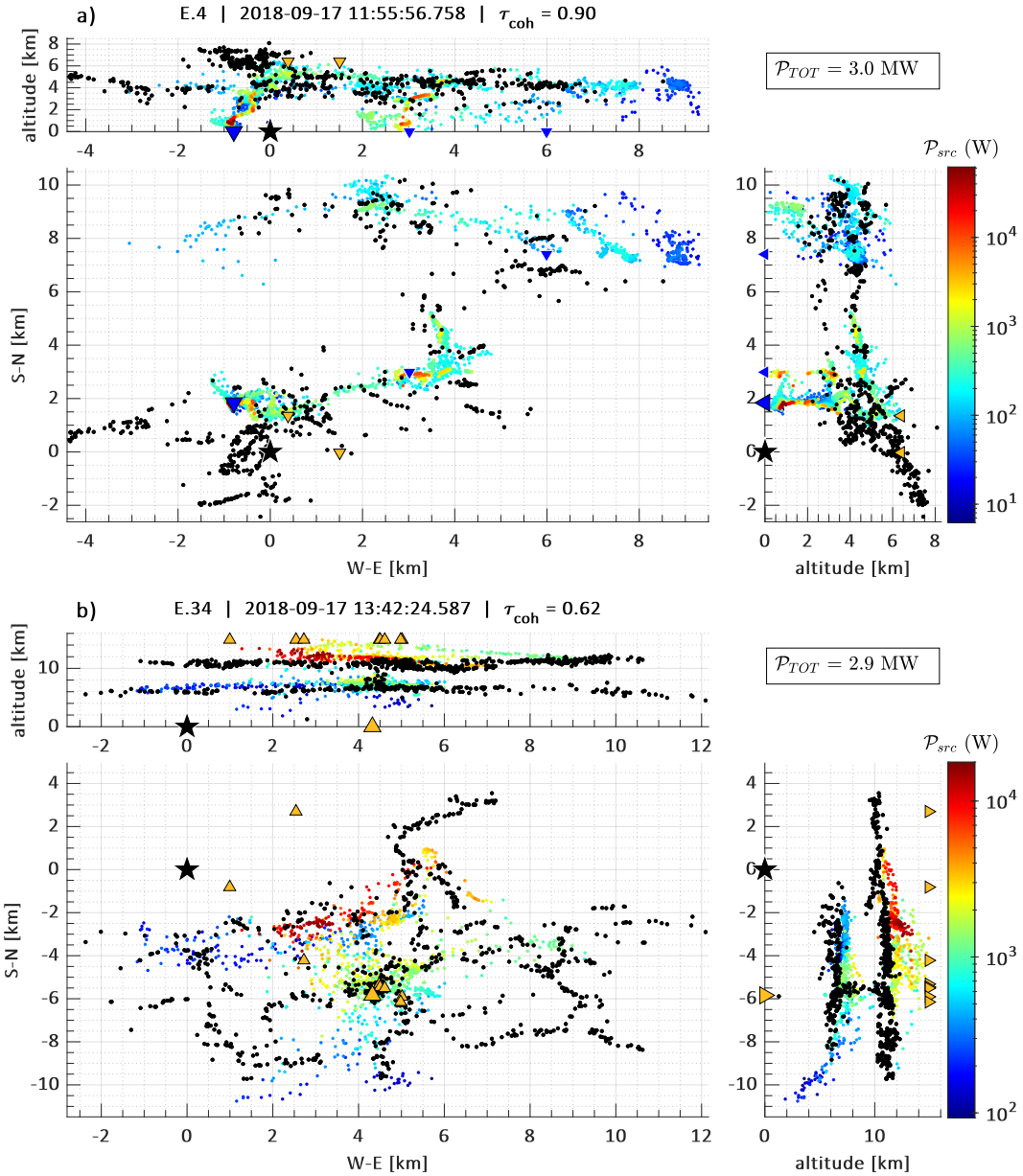

Figure 3: 3D acoustical reconstructions colored by the acoustical power of each source (colored dots). Météorage EM-LF ground detections (blue triangles for CGs, orange triangles for ICs, upward/downward for +/- peak current) and SAETTA EM-VHF detections (black dots). Symbol for Météorage reference detection is larger. IC symbols are arbitrarily located at top altitude in vertical projections, except for the reference one. Black star: acoustical array `AA` at the origin. For each event (a: E.4 - b: E.34) horizontal projection. Above it: West-East vertical projection. At its right: South-North vertical projection.

of 3D power mapping towards isolated sensors for EXAEDRE events described in Appendix B is shown in Figures S3 to S5.

Event S.8 (dated 2012-10-22 at 23:33:50.323, figure 4.a) is a +CG that gave rise to jellyfish sprites, analysed by Soula et al. (2015). Such events are labelled as +SPCGs (SP for "Sprites"). In EXAEDRE, no strong +CG comparable to this event was observed. Its total power is 52.4 MW, with a single reconstructed return stroke reasonably matching the main EUCLID CG ground detection. When comparing to the analysis of (Soula et al., 2015) (cf their figure 9 in section 4.2), one observes that acoustic detections are co-localized with almost all of the VHF detections occurring *before* the +SPCG event (blue and red dots on their figures 9.b and 9.e), with sources of highest acoustical power being co-localized with VHF detections just before the +SPCG (about 200 ms before, the red dots and the latest blue dots on their figures). This event also contains a second +SPCG stroke, with almost identical peak current (75.5 vs 75.7 kA), which is detected acoustically (see Figure S6 in Supporting Information) though it is quite distant from AA (29 km). For this second +SPCG, much less acoustical power is evaluated (3 MW), but this value is to be considered with caution given the large distance of observation (Gallin et al., 2016). No acoustical source is detected between the two +SPCG though VHF sources are observed. This may be due to a masking effect. The most powerful acoustic source (297 kW) is located within the lower charged layer, at 5.0 km in altitude (figure 4.a), in agreement with (Soula et al., 2015). This layer also contains most of the flash acoustical power. Nevertheless, powerful sources are also located within the reconstructed return stroke with maximum power 116 kW at 1.95 km in altitude. For the second +SPCG, peak of acoustical power is located around 7.6 km (see Figure S6 in Supporting Information) again in agreement with electromagnetic observations of (Soula et al., 2015).

The second event S.29 (dated 2012-10-26 at 20:35:58.856, figure 4.b) is a +IC of moderate total power 655 kW. The maximum point source power is 1.8 kW at 5 km in altitude, contrarily to event E.34. From East to West, one can distinguish first a source distribution inside the lower charged layer between 4 km and 6 km in altitude (the source of peak power is located at its easternmost). Then there is a vertical connection to the upper charged layer, occurring between 3 km and 5 km in the West direction of the array, with a significant proportion of acoustical power at the basis of this connection, down to 2 km in altitude. Then, an upper layer around 9 km in altitude extends Westward. Beyond 10 km in the West direction, there are detections in both layers and in between. The matching with HyLMA was already shown to be very satisfying by Gallin et al. (2016).

The third event (E.2 dated 2018-09-17 11:51:32.449, figure 4.c) is a -CG with a single reconstructed return stroke clearly matching the two very close -CG Météorage detections. The total acoustic power is 1.0 MW, close to average (see following section for a histogram of total power of all events). SAETTA reconstructions outline two charged layers extending in the eastern direction. The lower one, around 5 km altitude, is barely acoustically visible, while the top one (around 7 km altitude) is clearly reconstructed with a W-E extension of about 2 km. Another noteworthy feature is the presence of the most powerful source above 5 km in this positively charged upper layer with a peak value of 26.1 kW at 6.5 km. This is different from event E.4, for which most acoustical power was localized in the lower part of return strokes. This powerful source seems also to match the ground projection of a -IC Météorage detection (less than 500 m difference in both W-E and S-N directions). Below 5 km, the return stroke shows a tiny zone of powerful sources with a maximum value of 21.9 kW around 4 km in altitude, higher than for the previously studied E.4 event.

The fourth event (E.12 dated 2018-09-17 12:31:58.298, figure 4.d) is a +CG (peak current $I_{max} = +21.7$ kA). It shows a low total acoustic power of 241 kW, with the most powerful sources located in the upper part of the lighting flash, above 6 km in altitude. The maximum source power is only 1.3 kW at altitude 12.45 km. All sources below 4 km are extremely weak, less than 11 W. Despite this, there is a clear return stroke well lo-

calised with Météorage ground detection. Moreover, matching with SAETTA detections is excellent including the top layer at altitude between 10 km and 12 km. The connection between the two layers is visible both with SAETTA and acoustics, and matches several Météorage +ICs. The quality of the acoustical reconstruction of this event is remarkable despite its low acoustical power. This is also confirmed by the back-propagation to other sensors SA (see Supporting Information in Figure S4).

For the last detailed event (E.35 dated 2018-10-02 14:18:25.877, figure 4.e), three Météorage -CG return strokes are acoustically reconstructed (no IC detection was recorded by Météorage for this event). The one with the highest number of acoustical detections is the most westward one (i.e. the closest to AA). It corresponds to the third Météorage CG detection with the highest peak current and it is reconstructed down to the ground. For the remaining two, acoustic sources are identified only at altitudes above 1 km. There are also many more acoustical detections than SAETTA ones. The low number of VHF sources is explained by the compact flash structure which exhibits a rather limited vertical extension, and by the rather short duration of the VHF signal recorded by up to 9 VHF antennas. SAETTA VHF detections are almost all located in the SW quadrant relative to the main CG, at altitudes between 2.5 and 4.5 km in agreement with acoustic detections in this area. However, acoustics extends the identification of this lower layer in the north direction. The order of arrivals at AA is inverse to their emission time (see table S3 in Supporting Information). As for E.4 but contrarily to E.2, most powerful acoustical sources are located within the return stroke channel relatively near the ground (figure 3.b). Examining them according to their arrival time (which is also their position from West to East), the source of maximum power of the first one is 5.4 kW emitted at $Z = 973$ m, then 30.9 kW emitted at $Z = 1.62$ km for the second stroke, and 14.9 kW emitted at $Z = 735$ m for the last one. These last two strokes lead to the main peak of the RMS pressure at AA (see also figure S5 in Supporting Information). Above altitude 2.5 km all sources are of power less than 0.7 kW except two isolated points of power about 6.5 kW which cannot be clearly related to any return stroke.

4 Total acoustical power

4.1 Variability of the total acoustical power

We computed the total acoustical power $\mathcal{P}_{tot}$ for the 78 studied events (35 for SOP1: 24 -CGs, 9 +CGs and 2 ICs; 43 for EXAEDRE: 29 -CGs, 13 +CGs and 1 IC). Figure 5.a represents the distribution of its logarithm $M_P = log_{10}(\mathcal{P}_{tot})$. This distribution shows a reasonable agreement with a Gaussian distribution for M_P with a mean value of 5.96 and a standard deviation of 0.80. This corresponds for the acoustical power $\mathcal{P}_{tot}$ to a median power of about 0.91 MW with standard variations in the range 0.14 to 5.80 MW. All events previously examined are within that range, except event S.8, a powerful +SPCG. The main observation is the huge range of variation of the total power of the flashes, with slightly more than four orders of magnitude between the less energetic event (10.6 kW for E.13 -CG) and the most energetic one (165 MW for S.10 +CG). The most energetic event of EXAEDRE is E.33 (-CG) with 19.6 MW and the less energetic one of SOP1 is S.6 (+CG) with 79.8 kW. The three ICs (S.16, S.29, E.34) are in the middle range between 0.12 and 2.86 MW. The mean value of SOP1 events (11.73 MW) is about nine times larger than the one of EXAEDRE (1.36 MW). Indeed, the SOP1 campaign shows more energetic events than the EXAEDRE one, with 3 SOP1 events larger than 40 MW (all are +SPCGs) and none for EXAEDRE, and 13 SOP1 events larger than 3 MW (5 +SPCGs and 8 -CGs) compared to 4 EXAEDRE event (4 -CGs). On the contrary, EXAEDRE shows most of the low energy events (8 +CGs and 10 -CGs of less than 0.3 MW) compared to SOP1 (1 +CGs and 4 -CGs of less than 0.3 MW). In figure 5.b, these data are sorted in four categories:

- 8 +CGs generating sprites (Soula et al., 2015), labelled +SPCGs,

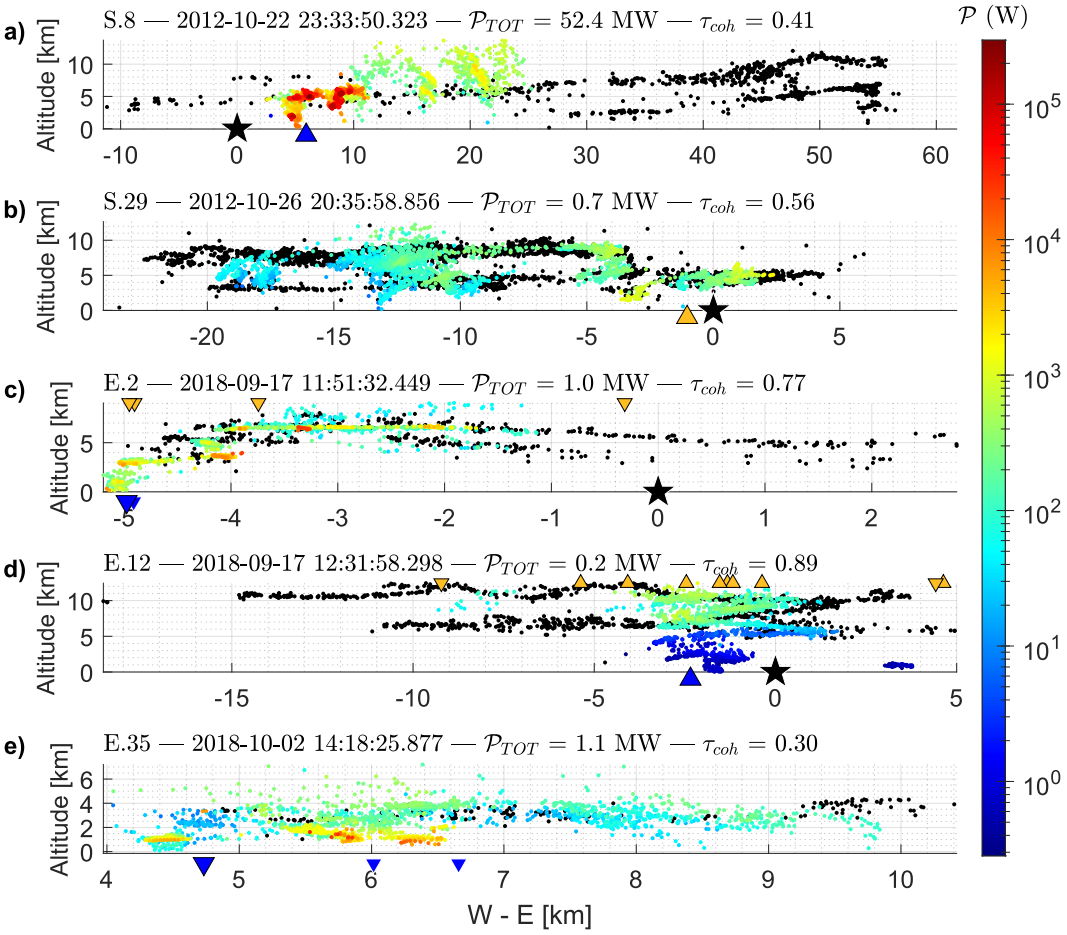

Figure 4: Same as 3 by with only West-East vertical projection. From top to bottom: events S.8, S.29, E.2, E.12 and E.35

- 50 typical CGs, labelled TCGs,
- 3 typical +ICs, labelled ICs,
- 17 events with ambiguous CG classification, labelled aCGs.

The first category contains events, all dated from 22-23 October 2012, which is a very specific storm which generated at least 12 sprite events (Soula et al., 2015) within a one hour and a half time span. Among these events, 8 of them were acoustically reconstructed (the other four occurred too far away to be detected acoustically). The second category includes 50 events (only -CGs, except S.1 and E.12 +CG events) from both SOP1 and EXAEDRE campaigns (25 events for both). Their acoustical reconstruction of at least one return stroke matched satisfyingly with Météorage or EUCLID locations. The third category contains the three +IC events S.16, S.29 and E.34. As this is a very low number of events, we chose to not include these ICs to the correlation computations and power law adjustments in section 5. The fourth category contains 17 CG events (all from EXAEDRE, 10 dated September 17, 2018 and 7 dated October 2, 2018, 12 +CGs and 5 -CGs) for which no clear return stroke could be reconstructed acoustically despite a ±CG classification. These ones are labelled as ambiguous (aCGs). We therefore chose to exclude them from the correlation computations and power law adjustments in the section 5. Figure 5.b outlines that typical CG events follow the average distribution, while +SPCG events are all above the median value and include the three most powerful events. Ambiguous events are more widespread but are mostly below the median power value and include the four less powerful ones. ICs are too few to draw any conclusion.

The overall observed variability of acoustical power over four orders of magnitude is comparable to the optical one. Lightning observation from satellite with a photodiode detector gives an optical power range of $[10^8-10^{12}]$ `W` (Kirkland et al., 2001), with a median value of 1 `GW` for 700,000 events. Even more powerful events (in the range $[10^{11}-10^{13}]$ `W`) were observed again from space by Turman (1977) and termed "superbolts". With VLF radio electric measurements, Holzworth et al. (2019) found the stroke energy spans over about 3 orders of magnitude above the mean energy (1 `kJ`). However, there are rare energetic events (above 1 `MJ`, less than 2% of occurrence), also named superbolts, associated to very high peak currents, larger than 150 `kA` in absolute value, for both negative and positive return strokes. They are observed surprisingly most frequently over the sea, especially in the eastern North Atlantic and Mediterranean and in periods (from November to January) of overall low electric activity. For our observation campaigns, both storms occurred during September and October, months of low superbolts probability. SOP1 events are all overland, and peak currents are all below 150 `kA` except for one event (S.14). Therefore, no superbolt is included in our database. Thus, even more powerful events from an acoustical point of view could be possible, and the observed four orders wide variability of acoustical power may be underestimated: for low values because of SNR issues, and for high values due to the lack of superbolts. Note that event E.33 (a -CG with the highest absolute peak current 115.7 `kA` for EXAEDRE and a large acoustical power) occurred over the sea, right to the eastern Corsica shore: though not a superbolt, it nevertheless shows that powerful events can occur over the sea.

When considering total acoustical energy $\mathcal{E}_{tot}$ (equation 6), it ranges between 4×10^{-4} `MJ` and 1 `MJ`. For TCG events it is limited between 1.4×10^{-3} `MJ` and 1.4×10^{-1} `MJ`, so over a span narrower than acoustical power and with no Gaussian distribution. To compare, Holmes et al. (1971) report an acoustical energy in the range 1 `MJ` to 17 `MJ` for 20 CG events measured with a frequency spectrum extending up to 500 or 650 `Hz` (depending on the day) without compensating for absorption nor density stratification. This is somewhat higher than our values, maybe due (i) to the larger bandwidth, (ii) to the fact that in our case we consider only the coherent part of the signal. Note that Holmes et al. (1971) deduce from these values the spectrum frequency peak according to Few's model (Few, 1969) and compare to the measured one, finding an acceptable agreement for negligible wind noise events. For this, they assume a conversion rate of 0.18% of to-

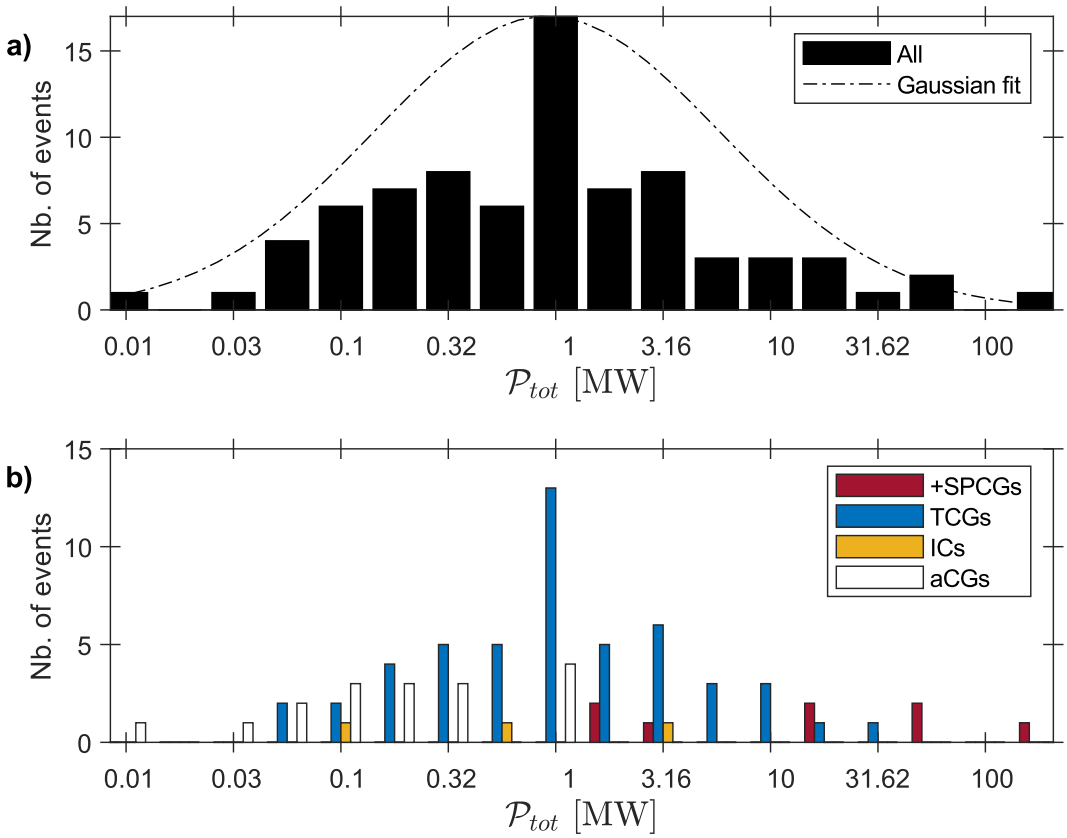

Figure 5: (a) Distribution of total power $\mathcal{P}_{tot}$ for all events, with a Gaussian fit (dash-dotted line). (b) Comparison of the distributions for powerful +CG events generating sprites (red), typical CG events (blue), +IC events (orange) or ambiguous events (white).

tal energy into acoustic one, and a stroke length of 4 km. The value of the conversion rate is controversial and is discussed in sections 11.2 and 11.3 of Rakov and Uman (2003). With almost the same method as Holmes et al. (1971), (Johnson et al., 2011) evaluates the total acoustical energy between 22 kJ and 2713 kJ in the [0.5−500] Hz band. Anderson et al. (2014) provide a much lower range between 0.2 and 12.6 kJ, estimated only from the very narrow band $[6-12]$ Hz, values compatibles with the ones from (Johnson et al., 2011) in the $[1-10]$ Hz band. These are to our knowledge the only direct evaluations of acoustical energy.

The WWLLN power $\mathcal{P}_{WLN}$ is derived from the energy $\mathcal{E}_{WLN}$ knowing the duration of the time window of measurement (1.33 ms). This power is compared to the total acoustical power for each studied event. The median value of the ratio $\frac{\mathcal{P}_{tot}}{\mathcal{P}_{WLN}}$ of the acoustic total power (in the range $[1-125]$ Hz) to the VLF total power (in the range [5−18] kHz) is found to be around 3.16. The first quartile is around 0.6 and the third quartile around 13 (excluding IC and ambiguous events). See Figure S11 in Supporting Information for the distribution of $\mathcal{P}_{WLN}$.

4.2 Comparison with previous methods

The signal process synthesised by equations 2, 3 and 5 is adapted from the method proposed by Holmes et al. (1971) and Johnson et al. (2011). There are however significant differences: (i) only signals detected as coherent are taken into account thanks to

PMCC analysis, (ii) the analysis by frequency bands allows to compensate for absorption, (iii) density stratification is taken into account, (iv) acoustical power is computed, in addition to energy. Moreover (v), in the method of Holmes et al. (1971), the energy of the signal measured by receiver at a time t is back-propagated to a single source at distance $c_0(t-t_{EM})$. This assumes implicitly that the emitted signal is of sufficiently high frequency (close to a $\delta-$Dirac function) so that there is no overlapping between the signal emanating from a source, and the signal emanating from a slightly closer source but having some finite duration. Obviously, this simplifying assumption cannot be satisfied for the low frequency part of the thunder sound signal that constitutes an important part of its content. This overlapping is taken into account by PMCC algorithm by considering time overlapping and by selecting coherent signal only.

Figure 6 quantifies the proportion of the signal energy found by PMCC algorithm to be coherent between the four sensors of `AA`, relative to the average of the signal energy measured by `AA` sensors

$$\tau_{coh} = \frac{4\sum_{coh}\left(\mathrm{P}^0\right)^2}{\sum_{j=1}^{4}\sum_{all}\left(\mathrm{P}^{0j}\right)^2}. \tag{7}$$

Here P^0 is the rms pressure found coherent by PMCC algorithm, while P^{0j} is the rms pressure derived from the raw signal measured by sensor $0j$ of the array. At the numerator, the summation is performed only for the coherent detections from PMCC (index $_{coh}$). At the denominator, it is done for all `(T,F)` couples (index $_{all}$). The result is then averaged over the four `AA` sensors (sum over j). This coherence level is plotted versus the ground distance to the main LLS detection, with one symbol for each storm. Colors indicate the received average frequency weighted by coherent acoustic energy received at the array

$$< \mathrm{F} >= \frac{\sum_{coh}\mathrm{F}\left(\mathrm{P}^0\right)^2}{\sum_{coh}\left(\mathrm{P}^0\right)^2}. \tag{8}$$

Obviously, one observes the coherence value is very dispersed. The median value is 0.65, but with extreme values between 0.04 and 0.92. Mostly, events from the storm of October 2, 2018 have a much lower coherence level (average 0.17 for ambiguous events, 0.25 for others) than those from September 17, 2018 (average 0.68 for ambiguous events, 0.72 for others) or from SOP1 (average 0.70). Among the events examined in details in section 3, we observe either high (E.4. E.12), median (E.2, E.34, S.29) and low (E.35, S.8) coherence values. The figure also indicates that incoherent events tend to have a lower average frequency. This likely shows that, as expected, higher frequencies are more likely to loose their coherence than lower ones. Also the array size is optimally tuned to frequencies around 10 `Hz`, and has been shown Lacroix et al. (2018) to detect less efficiently sources of higher frequency, especially in altitude. Also more powerful events tend to emit more intense high frequencies which therefore will have a better signal-to-noise ratio at the receiver and hence a higher coherency. However, some events very close to the sensor (less than 3 `km`) are of a relatively high frequency and get a low coherence level. This may be due to nearfield behavior linked to random tortuosity Lacroix et al. (2019). There is neither a clear link between coherence level and distance. Causes of low signal coherence may be signal masking by sources within the same flash (signals from two different thunder sources arrive at the same time), masking by ambient thunder noise from previous flashes (but this is unlikely for EXAEDRE October storm with very few events) or noise due to wind. For EXAEDRE, wind data (measured during the same time interval as analyzed sound signal and at the same place, see Large Table 1 in Supporting Information) indicate a somewhat stronger wind in October compared to September (its mean value was twice as high in the storm of October 2 as in that of September 17), but some September events nevertheless have a higher coherence level than October ones, for comparable wind levels. Whatever, the figure shows that coherency has to be considered as an important factor to analyze. Taking into account the entirety of the pres-

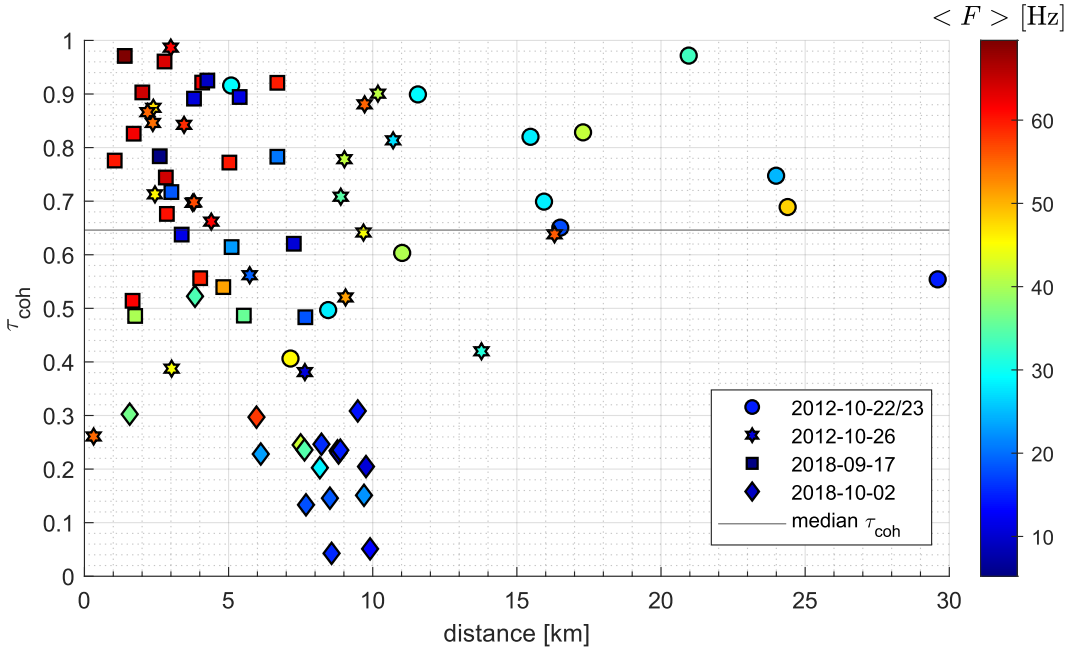

Figure 6: Coherence ratio versus ground distance, colored by mean frequency $< F >$. Circle and hexagram markers are for the SOP1 storms (respectively 2012-10-22 or 23 and 2012-10-26), square and diamond markers are for the EXAEDRE storms (respectively 2018-09-17 and 2018-10-02).

sure signal at a single microphone to compute energy may incorporate signal that can be uncertainly attributed to a single source within the flash.

Thanks to the combination of source identification and back-propagation, the influence of absorption and density stratification are taken into account by our method, contrarily to previous ones. Figure 7 quantifies the importance of these two effects by plotting the ratio of the total power computed when taking them into account, to the total power evaluated when omitting them. This ratio is always larger than one. For many events, it is between one and three, corresponding to most -CGs events whose power is located mainly within the return stroke (as for event E.4) and therefore at small or moderate altitudes (up to a few kilometers). Values can be however much higher for +SPCGs, +CGs, +ICs or some -CGs, for which power is mostly within the intracloud lower or upper layer (for event E.34 for instance), leading to ratio reaching almost 11. In all cases, the effect of density stratification is dominant over the one of standard absorption. The model of absorption is however limited to molecular relaxation. Absorption by cloud droplets (Baudoin et al., 2011) or scattering by atmospheric turbulence would further enhance the absorption, and therefore increase the source power when back-propagating signal. However these effects are difficult to quantify precisely, and are probably more sensitive at higher frequencies.

To summarize, this discussion shows that errors on power evaluation when not considering influence of correlation, stratification and absorption could typically range between an overestimation of a factor 10 of the thunder power (in the case of a low altitude flash with a coherence level of the order of 10%) to an underestimation of a factor 10 (high altitude flash with a coherence level of the order of 100%), e.g. two orders of magnitude uncertainty. Our method therefore significantly reduces this uncertainty. However it is not perfect: (i) part of the signal found to be incoherent by PMCC may be phys-

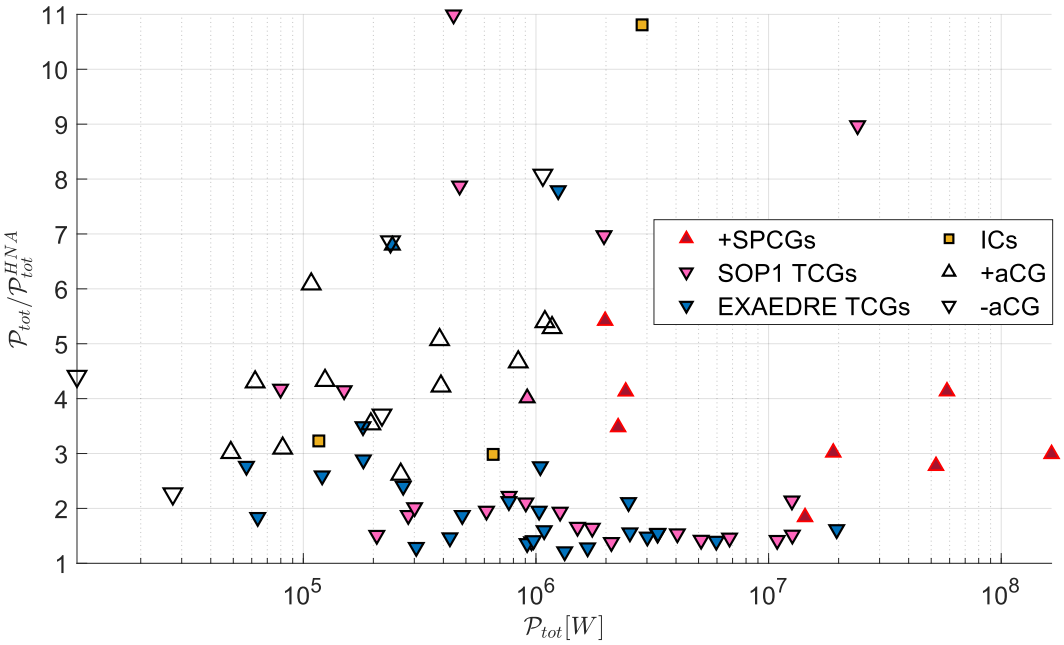

Figure 7: Ratio of total power $\mathcal{P}_{tot}$ computed by taking into account atmospheric absorption and density stratification to total power computed without taking into account them $\mathcal{P}_{tot}^{HNA}$, as function of total power. Red triangles for +SPCGs; magenta triangles for SOP1 TCGs; blue triangles for EXAEDRE TCGs; white triangles for EXAEDRE aCGs (upward/downward triangles for +CGs/-CGs), yellow squares for +ICs.

ical thunder signal, (ii) only density stratification is taken into account and not the one in speed of sound or wind, and (iii) absorption may be underestimated. Ways to further improve it are discussed in the conclusion.

5 Correlation between acoustical and electrical parameters

Theoretically, the electrical current $I(t)$ of a lightning can be related to the total energy per unit length E_l by the expression

$$E_l = \frac{1}{\pi R_0^2} \int_0^{t_d} \rho I^2 \, dt, \tag{9}$$

with R_0 the initial radius of the lightning channel, ρ the plasma resistivity and t_d the discharge duration. According to (Troutman, 1969) and (M. A. Uman et al., 1970), most of the total energy is used for the thermodynamic work of channel expansion, which is directly at the origin of the shock wave formation leading to thunder emission. Acoustical and electrical parameters are therefore expected to be fundamentally linked, so we can expect the variability of the acoustical power to be partly explained by the variability of some electrical quantities. Experimentally, Depasse (1994) observes the relationship

$$E_l = 2.2 \left[\int_0^{t_d} I^2 \, dt \right]^{0.64}, \tag{10}$$

with a correlation coefficient between these tow quantities equal to 0.76 (corresponding to a coefficient of determination $R^2 = 0.5$). This is obtained for 24 triggered lightning, triggering allowing to have a reliable measurement of $I(t)$ and E_l being measured accord-

Table 2: Coefficients of determination R^2 for linear regressions between the logarithms of the acoustical and the electric parameters. For $|I_{max}|$, the first value is when considering only events with a (i)CMC value, and the second value for all studied unambiguous CG events.

R^2	$\|iCMC\|$	$\|CMC\|$	$\|I_{max}\|$
$\mathcal{P}_{tot}$	0.53	0.56	0.57 / 0.61
$\mathcal{P}_{max}$	0.21	0.22	0.43 / 0.52
$\mathcal{E}_{tot}$	0.46	0.54	0.47 / 0.54
$\mathcal{E}_{max}$	0.33	0.43	0.35 / 0.38

Table 3: Synthesis of the correlations between the total acoustical power $\mathcal{P}_{tot}$ with peak current I_{max} and CMC. Coefficient of determination R^2, slope of the linear fit p, and considered number of events N for (i) +SPCG events, (ii) TCG events, (iii) both +SPCGs and TCGs.

$(R^2\ ;\ p\ ;\ N)$	+SPCGs	TCGs	Both
$\mathcal{P}_{tot}$ vs $\|I_{max}\|$	(0.23 ; 1.07 ; 8)	(0.59 ; 1.17 ; 50)	(0.61 ; 1.33 ; 58)
$\mathcal{P}_{tot}$ vs $\|CMC\|$	(0.70 ; 3.19 ; 8)	(0.36 ; 0.61 ; 25)	(0.56 ; 0.68 ; 33)

ing to Few's model Few (1969) by the peak of the frequency spectrum. Thunder signal is measured in the very nearfield at 70 m from the lightning channel. Due to triggering, it is likely that observed events are only -CGs.

In the present study, we only have access to the peak current $I_{max} = \max\left(I(t), 0 \leq t \leq t_d\right)$, and to the Charge Moment Change CMC which is proportional to the channel length and to the integrated current $\int_0^{t_d} I(t)\,dt$. Depasse (1994) also derived from measurements a relationship between the acoustic energy per unit volume E_{vol} measured at the microphone position and the peak current

$$E_{vol} = 1.31 \times I_{max}^{1.61}, \tag{11}$$

again with a coefficient of correlation of 0.76.

To establish correlations between acoustic and electric parameters, we consider all events from our database of natural flashes except the ambiguous ones. For these ones, we have doubts either on their signal-to-noise ratio, on the quality of their reconstruction or on their proper classification as CGs. The number of considered events is therefore 61, either ±CGs (and 3 +ICs) measured at distances up to a few tens of km. As parameters, we consider on the one side total acoustic power $\mathcal{P}_{tot}$, total acoustic energy $\mathcal{E}_{tot}$, peak of acoustic power $\mathcal{P}_{max}$ and peak of acoustic energy $\mathcal{E}_{max}$; and on the other side peak current I_{max}, charge moment change (CMC) and impulse charge moment change (iCMC). Table 2 collects the coefficients of determination R^2 for linear regression between the logarithms of these parameters. It shows that total values are always better correlated than peak ones, that total acoustical power is slightly better correlated than acoustic energy, and that CMC is always slightly better correlated than iCMC. This is why we focus the discussion on the total acoustical power versus CMC and peak current. Note that CMC corresponds to an integrated value describing the whole electric discharge (see section 1.1.3) and appears therefore more adapted than iCMC to a comparison with the total acoustical power.

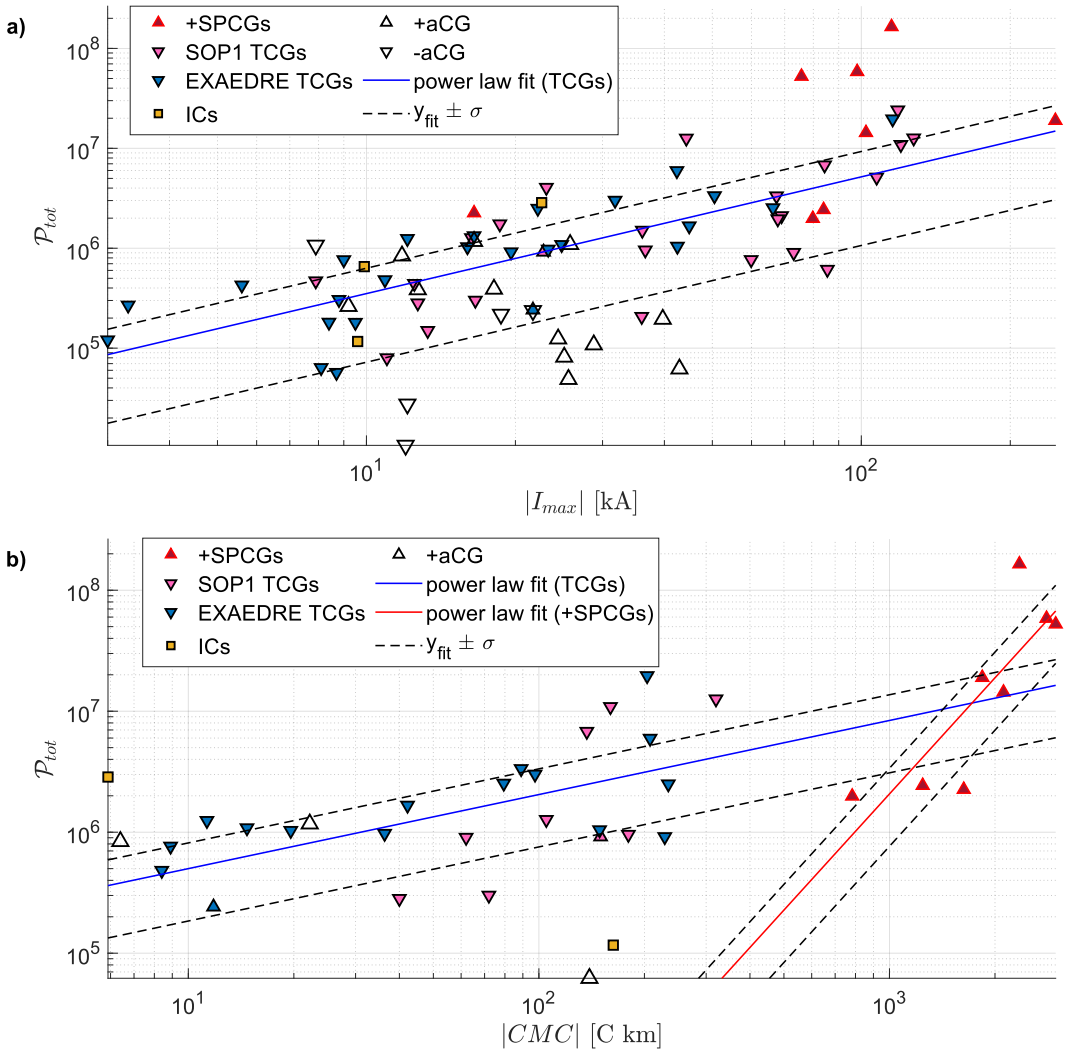

Figure 8: Acoustical power vs (a) absolute peak current or (b) absolute Charge Moment Change. Symbols: same as Fig.(7). Blue (resp. red) lines : fit with TCGs (resp. +SPCGs) events. Interval between dashed lines contains 68% of data.

In figure 8.a, the total acoustical power $\mathcal{P}_{tot}$ is represented as function of the absolute peak current $|I_{max}|$, provided by Météorage and EUCLID data for all 78 events. Figure 8.b, displays $\mathcal{P}_{tot}$ versus the absolute charge moment change $|CMC|$ for the 31 events (16 from SOP1 and 15 from EXAEDRE) for which this last quantity could be measured. For both cases, a linear regression on logarithmic scale is computed: (i) for the 8 +SPCG events, (ii) for the typical CGs, and (iii) for both categories. Results are summarized in table 3 where we provide the coefficient of determination R^2, the slope p of the linear fit, and the considered number of events N. The fits for TCGs are also visible in figure 8, and also the $\mathcal{P}_{tot}$ vs $|CMC|$ fit for +SPCGs only.

The results of these correlations between total acoustical power with either CMC or peak current enable us to notice that the correlations are similarly good for the two electrical parameters CMC and I_{max} when considering all the events (with respectively $R^2 = 0.56$ and $R^2 = 0.61$). However, this is likely not due to the same events: on the one hand, the total acoustical power of +SPCG events correlates significantly with their CMC ($R^2 = 0.70$), but poorly with their peak current. On the other hand, the total acoustical power of TCG events correlates badly with their CMC but significantly with their peak current ($R^2 = 0.59$). Moreover, for TCGs, the obtained power $p = 1.17$ of the correlation relation between acoustical power versus peak current is *very close* to the power $p = 1.21$ deduced from observations of Depasse (1994) (combining its equations (11) and (17) or Eq.(10)). Let us recall that in both cases an energetic quantity at the source is considered, either the injected energy per unit length E_l or, here, the acoustical power. This power differs from the value $p = 1.61$ (from Eq.11) observed for an energetic quantity at the receiver. We can therefore conclude that our results fully agree with those of Depasse (1994), but now for 50 natural TCGs lightning observed during four different storms at distances up to a few tens of `km`, in complement of 24 triggered lightning observed at 70 `m`. Our range of observed peak current is also slightly larger, between 3 `kA` and more than 100 `kA`, instead of a range 4.5 to 49.9 `kA` for Depasse (1994). The observed correlation for typical CGs is also coherent with reported correlations between the peak current and optical power measured either from the ground for triggered (Idone & Orville, 1985) and natural (Quick & Krider, 2013) lightning in the range [1−40] `kA`, or from space (Kikuchi et al., 2017) in the range [7−88] `kA`. However, I_{max} parameter alone cannot be sufficient to explain all observations, and in particular the deviations from the fit. The model of da Silva and Pasko (2014) (see their Figure 3a) shows a linear relationship between the acoustical pressure and the peak current, but with a slope highly dependant on the duration of the strong current phase (i.e the duration of the peak current sustain in the current temporal waveform). For a given I_{max} value, the pressure can vary by a factor 2.5. Their model is however limited to 2 `kA`, while our typical peak current values are about 10 to 100 times higher for most of the CG events. We therefore can expect even larger sensitivities to the detailed time dependency of the current.

The observed difference between TCGs and +SPCGs might be explained by the fact that the peak current measurement is known to undergo a higher uncertainty for positive discharges, whereas CMC is known for well describing the +SPCG events (Pasko et al., 2012). The good correlation between acoustical power and CMC was already noticed by Lacroix et al. (2018) for 7 of the present 8 +SPCGs. For these events, a fit was given for the acoustic energy per stroke length measured at the microphone position; therefore it did not compensate for effects of distance, absorption and density stratification. Nevertheless, the obtained value of power $p = 4$ of CMC is not very different from the present power $p = 3.19$. We also observe that CMC values of all +SPCG events (in the range 780 to 2980 `C km`) are one or two orders of magnitude larger than CMCs of all other events (in the range 8 to 320 `C km`). We can conclude that I_{max} is the most efficient electrical parameter we get to describe the typical CGs. For +SPCGs, it is more difficult to conclude given the small number of events. However, it provides an indication that CMC may be a parameter of interest for +SPCG events.

We can complement this analysis by comparing the correlation between the total acoustical power and the peak current for events with a total acoustical power either larger or smaller than 1 MW. By doing so, we obtain respectively $R^2 = 0.50$ and $R^2 = 0.04$. It might mean that events of lowest power are more difficult to estimate acoustically due to their low SNR. However, most of these low power events are of ambiguous classification and some of them could be indeed ICs for which we could expect also a different behavior from CGs. Several ambiguous events (and also two of our three certain +ICs) are nevertheless within the range of uncertainty (within the dashed lines of figure 8.a) $y_{fit} \pm \sigma$ with $\sigma = \delta \times y_{fit}$, δ being the relative difference. This value $\delta = 0.8$ is chosen so that 68% of the data are within this interval. A few more ambigous events (and also +IC E.34) are even above the upper bound, as do also five of the 8 +SPCGs. Note that this value of δ means an error ratio between $1 - \delta = 0.2$ and $1 + \delta = 1.8$. This is consistent with the results of Appendix B where one observes a ratio of measured to reconstructed peak pressures in the range [0.5−1.5], so in the range [0.25−2.25] for acoustical power. Finally, one can note that the VLF power from WWLLN is known for being a good estimator of the peak current value - see equation 2 in (Hutchins et al., 2012), confirmed by figure S12 in Supporting Information for our data (with $R^2 = 0.73$). However, although total acoustical power correlates well with peak current, it does not correlate so clearly with VLF power, with an R^2 coefficient equal to 0.36 only (see figure S13 in Supporting Information). Consequently, total VLF power cannot be a good direct estimator of the total acoustical power.

Conclusion

Acoustic data from EXAEDRE campaign in Corsica (2018) are analysed for two storms, much more active than those previously studied (SOP1, Cévennes, 2012). Using standard methods of acoustical source detection in addition to electromagnetic reconstruction (VHF) and ground impact localization (LF), we are able to reconstruct the 3D spatial distribution of sound sources of a lightning flash and compensate for the main propagation effects (spherical spreading, attenuation and density exponential stratification). Assuming each detection is a point source, we estimate the distribution of acoustical power within a large number (78) of natural flash events. We also show the importance of considering only coherent field in the microphone signals, and of compensating sound absorption and (most important) density stratification. In some cases, energy of coherent signal can be less than 10% of the total one, while density stratification increases the source power by a ratio of 10 when power peak is located in upper charged layer.

We therefore propose here a 4D reconstruction of lightning flashes, adding the physical variable of acoustical power to the 3D geometrical position of the sources. This allows us to analyze firstly the distribution of the total power of each event. It spans over more than four orders of magnitude (from 10.6 `kW` to 165 `MW`), similarly to previous observations in optics and electromagnetics. Secondly, the spatial distribution of the radiated power inside each event appears highly variable. Some events are quite homogeneous. However, for a majority of cases, acoustical power is very localized in tiny sections of the return stroke channel. This observation contradicts the common hypothesis used for thunder models of homogeneous distribution of acoustical energy inside flashes (Few, 1969; Ribner & Roy, 1982; Anderson et al., 2014; Lacroix et al., 2019). Other events also show a localization of acoustical power rather in the intracloud layers.

The total acoustical power of flashes shows a reasonably good correlation with some electromagnetic parameters. First, for most CG events, we observe a good correlation with peak current. This therefore agrees with literature results obtained either for a smaller number of triggered flashes (Depasse, 1994) or for a single triggered event leading to successive discharges (Wang et al., 2022). Except for two cases, all the +CG events we observe are acoustically powerful events, that gave rise to sprites (Soula et al., 2015). For this group, correlation is observed with Charge Moment Change, in agreement with a

previous observation (Lacroix et al., 2018). For this type of events, correlation with peak current turns out very weak, as does correlation with CMC for typical -CGs. The number of observations for this kind of rare events, is however limited to 8 cases only, and further data would be necessary. Similarly, ascertained ICs are too few to establish any correlation with electrical parameters. There finally remains the group of ambiguous events (initially classified by LLS analysis as CGs but with no clear acoustical ground connection). These ones are generally of lower acoustical power, do not show a clear correlation with the peak current, and have a too small CMC to be measurable.

Future research will aim to improve the 4D reconstruction of the flashes on the one side, and to better understand the power variability on the other side. The use of several acoustic arrays instead of one will allow to perform 4D reconstruction under various observation angles. This could enable us to either better understand the influence of propagation effects (mostly wind and temperature gradients, and wind bursts), or to compensate for it by an averaging process. Another unknown meteorological effect is the absorption by water droplets or by ice in clouds, which is suspected to increase sound absorption (Baudoin et al., 2011) and therefore acoustical power, but which needs experimental validation. Increasing the bandwidth of acoustic measurements in the high frequency range will provide a more precise localization and quantification of the acoustical power. In particular, according to Few's model (Few, 1969), it will better capture the frequency peak of events of low intensity such as intracloud flashes. This could be done by designing arrays of various sizes adapted to various frequency ranges. Acoustical 4D reconstruction could be also complemented by optical measurements with the aim to detect local variations of temperature within return strokes. The use of several sensors could also provide a better understanding of the variation of thunder amplitude or energy with distance of observation. Improved models of thunder will be useful to understand its correlation with various electrical parameters, including some not explored here (for instance current versus time instead of simply peak current, or local conductivity). These models may be specific for different types of flashes (-CGs, +CGs, +SPCGs, ICs, superbolts...) and should be able to predict the observed heterogeneous distribution of acoustical power.

Acknowledgements

The authors are grateful to Eric Defer, Ronan Houel (both from Laboratoire d'Aérologie - Observatoire Midi Pyrénées, Toulouse, France) and Stéphane Pédeboy (Météorage, France) for fruitful discussions. They also thank Guénolé Miancien (CEA, DAM, DIF) for his work on the localization accuracy of acoustic reconstructions of lightning in the context of an engineering internship. Authors thank the World Wide Lightning Location Network (http://wwlln.net), a collaboration among over 50 universities and institutions, for providing the lightning location data used in this paper. The authors acknowledge the CEA for supplying the data and the HyMeX database teams (ESPRI/IPSL and SEDOO/OMP) for their help in accessing the data. HyLMA data were obtained from the HyMeX program, sponsored by Grants MISTRALS/HyMeX and ANR-11-BS56-0005 IODA-MED project. JM acknowledges support from the National Science Centre, Poland, for development of the ELF measurement system under grant 2015/19/B/ST10/01055.

Data Availability Statement

Following data are available online. SOP1 acoustic data: (Farges, 2023b); EXAEDRE acoustic data: (Farges, 2023a); SOP1 LMA data: (Rison, 2012); EXAEDRE LMA data: (Defer et al., 2021); SOP1 lightning data: (Schulz, 2013).

EXAEDRE Météorage data and CMC and iCMC data are provided in Large Table S1 in Supporting Information.

band	F_{min} [Hz]	F_{max} [Hz]	F [Hz]	δT[s]
1	1.000	1.202	1.101	8.2
2	1.202	1.445	1.324	6.9
3	1.445	1.738	1.592	5.9
4	1.738	2.089	1.914	5.0
5	2.089	2.512	2.301	4.2
6	2.512	3.020	2.766	3.6
7	3.020	3.631	3.325	3.1
8	3.631	4.365	3.998	2.7
9	4.365	5.248	4.807	2.3
10	5.248	6.310	5.779	2.0
11	6.310	7.586	6.948	1.8
12	7.586	9.120	8.353	1.6
13	9.120	10.965	10.042	1.4
14	10.965	13.183	12.074	1.3
15	13.183	15.849	14.516	1.2
16	15.849	19.055	17.452	1.1
17	19.055	22.909	20.982	1.0
18	22.909	27.542	25.225	1.0
19	27.542	33.113	30.328	1.0
20	33.113	39.811	36.462	1.0
21	39.811	47.863	43.837	1.0
22	47.863	57.544	52.704	1.0
23	57.544	69.183	63.364	1.0
24	69.183	83.176	76.180	1.0
25	83.176	100.000	91.588	1.0

Table A1: Detailed parameters for PMCC frequency bands and time windows used in this work.

Appendix A PMCC configuration

We detail the configuration of the PMCC algorithm used with the SOP1 and EXAEDRE data analysed in the presented work. As shown in section 2.1, the cross-correlation analysis on the signals measured by the four sensors is performed after frequency-filtering them. Chebyshev bandpass filters of order 2 between F_{min} and F_{max} are used, with a ripple of 0.01 dB within the useful narrow-band. The frequency bands are logarithmically distributed from 1 to 100 Hz as shown on Table A1, giving F_{min}, F_{max} and the mean frequency F (chosen for computing the absorption). The cross-correlation calculations are performed on sliding time windows whose duration (δT) varies as a function of F. The last column of Table A1 also gives these durations. Two successive time windows associated to a given frequency band have an overlap ratio of 90%. The high overlapping rate of time windows allows a high sampling rate of the signal. A Chebyshev filter for frequency windows enables PMCC algorithm to detect a high number of coherent sources. As a counterpart, the frequency bands overlap significantly : for each band, the filter value approaches one between $\mathtt{F}_{min}$ and $\mathtt{F}_{max}$, but decays smoothly beyond. These choices are similar to those of Lacroix et al. (2018). The PMCC output RMS pressure amplitudes, amplified due to this overlapping, are compensated according to the method described in Garces (2013) to avoid any overestimation.

Appendix B Using acoustic power mapping to evaluate thunder

One application of the 3D acoustic power mapping proposed in this work is to evaluate when and how thunder signals are measured at isolated sensors, here the 8 isolated sensors SA described in section 1.1.1 and all located within a 10 km radius of AA. By inverting the process of back-propagating the RMS coherent pressure measured in AA to its acoustical source, we can also then forward-propagate it from the source to any sensor SA and predict there the envelope of the RMS pressure, compared to the actual measurement. Here, the purpose is not to obtain a perfect matching, since the propagation remains simplified and the isolated microphones could receive other signals from coherent or incoherent nearby acoustical sources. But we intend to recover some key properties of the predicted envelope in the measured one. This process is illustrated for the events E.4 in figure B1 and E.34 in figure B2, and in figures S3 to S5 in Supporting Information for events E.2, E.12 and E.35.

With the same assumptions as for back-propagation, one deduces from each coherent pressure signal $\mathtt{P}^0$ measured at AA for a given time window and frequency band, its corresponding value at sensor $\mathtt{SA}_n$

$$\mathtt{P}^n = \frac{r_0}{r_n}\sqrt{\frac{\rho_0(z_0)}{\rho_0(z_n)}}\exp\left(-\alpha \times (r_n - r_0)\right) \times \mathtt{P}^0, \tag{B1}$$

where z_n is the altitude of sensor $\mathtt{SA}_n$ and $z_0 = 38$ m the one of AA. The highest sensor is at 258 m, so the effect of density stratification is negligible in this case, but not the one of atmospheric absorption.

The arrival time T^n and the distance r_n from the source to the sensor are linked by the relation

$$T^n = t_{EM} + \frac{r_n}{c_0} = T + \frac{r_n - r_0}{c_0}. \tag{B2}$$

For a given time T^n, the envelope value is obtained as the quadratic sum of P^n pressures over all frequency bands. This process is illustrated for the event E.4 in figure B1. For all sensors AA and $\mathtt{SA}_n$ ($n = 1$ to 8), the reconstructed and measured RMS pressure envelopes are represented (black line for the estimation, magenta for the measurement). For each sensor, we indicate its ground distance and its azimuth relative to the main Météorage detection. We also present a top view of the location of the various sensors and of the reconstructed sources colored by their acoustical power $\mathcal{P}$ (in Watt) defined by equation 3. We observe a reasonably good agreement between the measured and reconstructed envelopes in terms of general shapes. For amplitudes, the ratio of the reconstructed to measured main peaks is between 0.94 (station AA) and 1.96 (station $\mathtt{SA}_2$), which is acceptable given the many uncertainties and simplifying assumptions we made. Only at the relatively distant microphones $\mathtt{SA}_6$ and $\mathtt{SA}_7$ is the reconstructed signal strongly overestimated. Note also that sensors 1 to 6 are situated in the foothills of Corsica mountains that are here around 800 m high in this region. Topography effects may perturb the propagation, especially for event E.4, for which the peak of sound power is located only around one kilometer above sea level. We can observe that the agreement on the amplitudes of the remaining part of the RMS envelope after the first peak is also satisfactory, and that all measured secondary peaks are also predicted for $\mathtt{SA}_n$ sensors. One can however observe that some predicted secondary peaks are not clearly measured, especially when immediately following the main peak (see for instance $\mathtt{SA}_3$, $\mathtt{SA}_4$, $\mathtt{SA}_1$).

Some noticeable results are also presented for events E.34 on figure B2. This IC event is acoustically less intense than the previous -CG, leading to measured amplitudes in the range around 0.1 to 0.2 Pa compared to values up to 4 Pa for event E.4. These overall levels are nevertheless reasonably well recovered by the reconstruction except at sensors 6, 7 and 8. Sensors 7 and 8 are just beneath the flash (see [ref explaining why

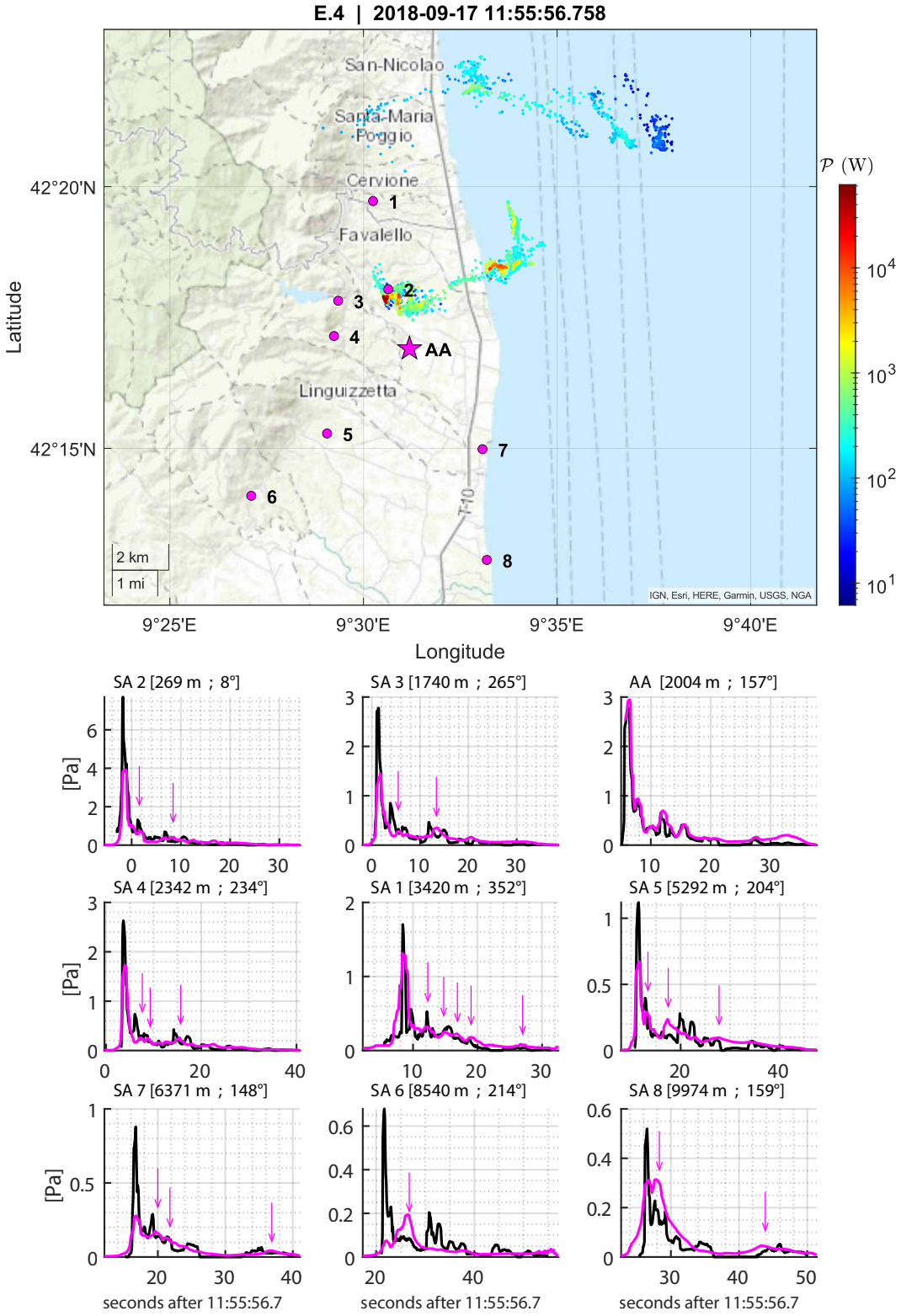

Figure B1: For event E.4, on top: map with position of isolated sensors `SA` (magenta circles), acoustic array `AA` (magenta star) and horizontal projection of each reconstructed source point (colored by its acoustic power, colorbar in logarithmic scale). On bottom: comparison between the RMS pressure envelopes of measured signal ($\tilde{p}_n$, magenta) and of reconstructed sources ($\tilde{\mathrm{P}}_n$, black). Magenta arrows point main measured secondary arrivals at `SA`.

Table B1: Table of timeshifts δt_n (in second) for which the envelopes show the best comparison.

event	AA	$\mathtt{SA}_1$	$\mathtt{SA}_2$	$\mathtt{SA}_3$	$\mathtt{SA}_4$	$\mathtt{SA}_5$	$\mathtt{SA}_6$	$\mathtt{SA}_7$	$\mathtt{SA}_8$
E.4	0	1.6	3.9	4	3	3.6	2.6	1.5	1.9
E.34	0.3	2.8	2.9	2.8	1.6	1.3	-2	-1.1	6

this relative source-array location is unfavorable for detection]), and sensor 6 is in the most mountainous region. The reconstruction also predicts two main peaks. This double peaked structure is clearly observed at sensor $\mathtt{SA}_2$. At the most distant sensor $\mathtt{SA}_1$ the phase difference between the two predicted peaks is reduced so that they tend to merge, in agreement with observation. However, for all presented microphones including AA, earlier arrivals are measured but not well reconstructed. From AA we know they likely emanate from the closest reconstructed sources south of it (blue dots on figure 3.b, for $x <$ 2 km on horizontal projection). Assuming the amplitude of these sources is underestimated by the reconstruction, it may explain observed earlier arrivals, except at sensor $\mathtt{SA}_8$. As a summary for this event, one can conclude that despite the relatively low signal amplitudes and small level of coherency, all RMS peaks derived from AA coherent reconstruction are indeed measured by SA sensors, though the opposite is not true.

Mismatches observed for some sensors were expected as our propagation model is simplistic because it neglects temperature and wind gradients which obviously are all the more important in a stormy atmosphere, uses a simple model of atmospheric absorption and neglects influence of topography. In particular, atmospheric gradients are difficult to predict (or even measure) at the small scales necessary to propagate acoustic waves in the wavelength range 3.4 m (at 100 Hz) to 340 m (at 1 Hz). Also strong local wind gusts are likely to occur and may induce important noise at some microphones, thus degrading the SNR. It is important to note that these envelopes have been time shifted of a quantity δt_n to compensate for the main propagation uncertainties of the model: (i) the slight desynchronization of various sensors $\mathtt{SA}_n$ relative to AA, (ii) the errors on Météorage localization (which can extend up to 1 km), (iii) the value of the sound speed, (iv) the atmospheric heterogeneities in wind and temperature. The time shifts δt_n are computed for each sensor $\mathtt{SA}_n$ by fitting the reconstructed and measured times of arrival (TOA) of the main peaks of each event. Time delays δt_n are given in table B1 for the E.4 and E.34 events. Note this is the only adjustable parameter. The mean value of the time shift is +2.04 s. The fact that it is positive is consistent with the mean temperature decay with altitude: actual sound speed is likely to be overestimated by ground sound speed. Hence, the reconstructed signal arrives too early and has to be time shifted with a positive δt_n. Assuming (i) a typical propagation distance between AA and source plus between source and SA of 12 km, (ii) sources mostly between 0 and 10 km of altitude, (iii) a temperature decay of 6.5 K/km, this leads to an average sound speed of about 330 m/s instead of 350 m/s and to a time shift equal to 2.08 s, comparable to the average value.

To summarize, the proposed method of 3D acoustic pressure mapping is shown in this appendix to efficiently evaluate with a reasonable accuracy the pressure variations within a 10 km range around the main acoustical array. Moreover, isolated sensors can complement the information from this array.

References

Anderson, J. F., Johnson, J. B., Arechiga, R. O., & Thomas, R. J. (2014, Decem-

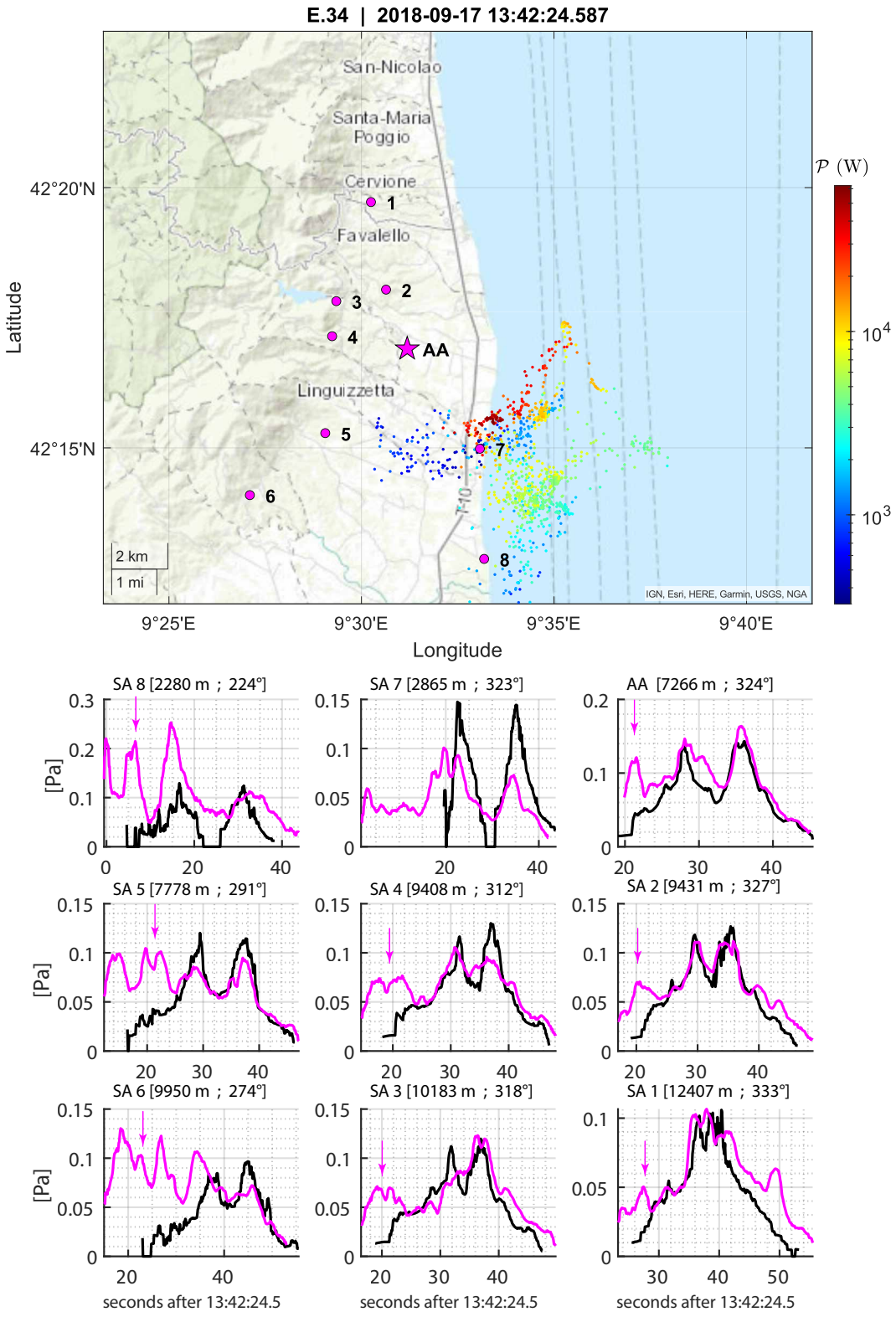

Figure B2: Same legend as bottom of figure B1 for event E.34. Magenta arrows point measured peaks which are not predicted by the forward propagation to `SA` and poorly detected by PMCC at `AA`.

ber). Mapping thunder sources by inverting acoustic and electromagnetic observations. *Journal of Geophysical Research: Atmospheres*, *119*(23), 13,287–13,304. doi: 10.1002/2014JD021624

Arechiga, R. O., Johnson, J. B., Edens, H. E., Thomas, R. J., & Rison, W. (2011, May). Acoustic localization of triggered lightning. *Journal of Geophysical Research*, *116*(D9), D09103. doi: 10.1029/2010JD015248

Attenborough, K. (1985, April). Acoustical impedance models for outdoor ground surfaces. *Journal of Sound and Vibration*, *99*(4), 521–544. doi: 10.1016/0022-460X(85)90538-3

Bass, H. E. (1980). The propagation of thunder through the atmosphere. *The Journal of the Acoustical Society of America*, *67*(6), 1959. doi: 10.1121/1.384354

Baudoin, M., Coulouvrat, F., & Thomas, J.-L. (2011, September). Sound, infrasound, and sonic boom absorption by atmospheric clouds. *The Journal of the Acoustical Society of America*, *130*(3), 1142–1153. doi: 10.1121/1.3619789

Berger, K. (1975). Parameters of lightning flashes. *Electra*, *80*, 223-237.

Blokhintzev, D. (1946, October). The propagation of sound in an inhomogeneous and moving medium i. *The Journal of the Acoustical Society of America*, *18*(2), 322–328. doi: 10.1121/1.1916368

Brode, H. L. (1959, March). Blast Wave from a Spherical Charge. *The Physics of Fluids*, *2*(2), 217–229. doi: 10.1063/1.1705911

Cansi, Y. (1995). An automatic seismic event processing for detection and location: The P.M.C.C. Method. *Geophysical Research Letters*, *22*(9), 1021–1024. doi: 10.1029/95GL00468

Cansi, Y., & Le Pichon, A. (2008). Infrasound Event Detection Using the Progressive Multi-Channel Correlation Algorithm. In D. Havelock, S. Kuwano, & M. Vorlnder (Eds.), *Handbook of Signal Processing in Acoustics* (pp. 1425–1435). New York, NY: Springer. doi: 10.1007/978-0-387-30441-0_77

Coquillat, S., Defer, E., de Guibert, P., Lambert, D., Pinty, J.-P., Pont, V., ... Rison, W. (2019, November). SAETTA: high-resolution 3-D mapping of the total lightning activity in the Mediterranean Basin over Corsica, with a focus on a mesoscale convective system event. *Atmospheric Measurement Techniques*, *12*(11), 5765–5790. doi: 10.5194/amt-12-5765-2019

Cummer, S. A., & Lyons, W. A. (2004). Lightning charge moment changes in U.S. High Plains thunderstorms. *Geophysical Research Letters*, *31*(5). doi: 10.1029/2003GL019043

da Silva, C. L., & Pasko, V. P. (2014). Infrasonic acoustic waves generated by fast air heating in sprite cores. *Geophysical Research Letters*, *41*(5), 1789–1795. doi: 10.1002/2013GL059164

Dawson, G. A., Richards, C. N., Krider, E. P., & Uman, M. A. (1968). Acoustic output of a long spark. *Journal of Geophysical Research (1896-1977)*, *73*(2), 815–816. doi: 10.1029/JB073i002p00815

Defer, E., Pinty, J.-P., Coquillat, S., Martin, J.-M., Prieur, S., Soula, S., ... Molini, G. (2015, February). An overview of the lightning and atmospheric electricity observations collected in southern France during the HYdrological cycle in Mediterranean EXperiment (HyMeX), Special Observation Period 1. *Atmospheric Measurement Techniques*, *8*(2), 649–669. doi: 10.5194/amt-8-649-2015

Defer, E., Prieur, S., & Coquillat, S. (2021). *L1 saetta science data.* Aeris. Retrieved from `https://en.aeris-data.fr/landing-page/?uuid=9be8ac89-1fa5-49d1-b723-c30d94ca10a1` doi: 10.25326/236

Depasse, P. (1994). Lightning acoustic signature. *Journal of Geophysical Research*, *99*(D12), 25933. doi: 10.1029/94JD01986

Drobinski, P., Ducrocq, V., Alpert, P., Anagnostou, E., Branger, K., Borga, M., ... Wernli, H. (2014, July). HyMeX: A 10-Year Multidisciplinary Program on the Mediterranean Water Cycle. *Bulletin of the American Meteorological Society*,

95(7), 1063–1082. doi: 10.1175/BAMS-D-12-00242.1

Ducrocq, V., Braud, I., Davolio, S., Ferretti, R., Flamant, C., Jansa, A., ... Tamayo, J. (2014, July). HyMeX-SOP1: The Field Campaign Dedicated to Heavy Precipitation and Flash Flooding in the Northwestern Mediterranean. *Bulletin of the American Meteorological Society*, *95*(7), 1083–1100. doi: 10.1175/BAMS-D-12-00244.1

EXAEDRE. (2018). Retrieved 2022-10-20, from `https://www.hymex.org/exaedre/`

Farges, T. (2023a). *Acoustic array.* Mistrals. doi: 10.6096/6004

Farges, T. (2023b). *Microphone network.* Mistrals. doi: 10.6096/6003

Few, A. A. (1969, December). Power spectrum of thunder. *Journal of Geophysical Research*, *74*(28), 6926–6934. doi: 10.1029/JC074i028p06926

Few, A. A. (1970, December). Lightning channel reconstruction from thunder measurements. *Journal of Geophysical Research*, *75*(36), 7517–7523. doi: 10.1029/JC075i036p07517

Few, A. A., Dessler, A. J., Latham, D. J., & Brook, M. (1967). A dominant 200-hertz peak in the acoustic spectrum of thunder. *Journal of Geophysical Research (1896-1977)*, *72*(24), 6149–6154. doi: 10.1029/JZ072i024p06149

Few, A. A., & Teer, T. L. (1974, November). The accuracy of acoustic reconstructions of lightning channels. *Journal of Geophysical Research*, *79*(33), 5007–5011. doi: 10.1029/JC079i033p05007

Gallin, L., Farges, T., Marchiano, R., Coulouvrat, F., Defer, E., Rison, W., ... Nuret, M. (2016, April). Statistical analysis of storm electrical discharges reconstituted from a lightning mapping system, a lightning location system, and an acoustic array. *Journal of Geophysical Research: Atmospheres*, *121*(8), 3929–3953. doi: 10.1002/2015JD023745

Garces, M. A. (2013, June). On Infrasound Standards, Part 1 Time, Frequency, and Energy Scaling. , *2013*. doi: 10.4236/inframatics.2013.22002

Glassner, A. (2000, March). The digital ceraunoscope: synthetic thunder and lightning. I. *IEEE Computer Graphics and Applications*, *20*(2), 89–93. doi: 10.1109/38.824552

Hill, R. D. (1968). Analysis of irregular paths of lightning channels. *Journal of Geophysical Research (1896-1977)*, *73*(6), 1897–1906. doi: 10.1029/JB073i006p01897

Holmes, C. R., Brook, M., Krehbiel, P., & McCrory, R. (1971). On the power spectrum and mechanism of thunder. *Journal of Geophysical Research (1896-1977)*, *76*(9), 2106–2115. doi: 10.1029/JC076i009p02106

Holzworth, R. H., McCarthy, M. P., Brundell, J. B., Jacobson, A. R., & Rodger, C. J. (2019). Global Distribution of Superbolts. *Journal of Geophysical Research: Atmospheres*, *124*(17-18), 9996–10005. doi: 10.1029/2019JD030975

Hutchins, M. L., Holzworth, R. H., Rodger, C. J., & Brundell, J. B. (2012, August). Far-Field Power of Lightning Strokes as Measured by the World Wide Lightning Location Network. *Journal of Atmospheric and Oceanic Technology*, *29*(8), 1102–1110. doi: 10.1175/JTECH-D-11-00174.1

ICAO. (1993). *Manual of the ICAO standard atmosphere: extended to 80 kilometres (262 500 feet)* (Vol. 7488). International Civil Aviation Organization.

Idone, V. P., & Orville, R. E. (1985). Correlated peak relative light intensity and peak current in triggered lightning subsequent return strokes. *Journal of Geophysical Research: Atmospheres*, *90*(D4), 6159-6164. doi: https://doi.org/10.1029/JD090iD04p06159

ISO 9613-1. (2003). Retrieved from `https://www.iso.org/obp/ui/#iso:std:iso:9613:-1:ed-1:v1:en`

Johnson, J. B., Arechiga, R. O., Thomas, R. J., Edens, H. E., Anderson, J., & Johnson, R. (2011). Imaging thunder. *Geophysical Research Letters*, *38*(19). doi: 10.1029/2011GL049162

Kikuchi, H., Sato, M., Ushio, T., Morimoto, T., Kikuchi, M., Yamazaki, A., ... Kawasaki, Z. (2017). Simultaneous observations of optical lightning from space and LF band lightning waveforms from the ground. *Geophysical Research Letters*, *44*(2), 1123–1131. doi: 10.1002/2016GL071783

Kirkland, M. W., Suszcynsky, D. M., Guillen, J. L. L., & Green, J. L. (2001). Optical observations of terrestrial lightning by the FORTE satellite photodiode detector. *Journal of Geophysical Research: Atmospheres*, *106*(D24), 33499–33509. doi: 10.1029/2000JD000190

Krider, E. P., Dawson, G. A., & Uman, M. A. (1968). Peak power and energy dissipation in a single-stroke lightning flash. *Journal of Geophysical Research (1896-1977)*, *73*(10), 3335–3339. doi: 10.1029/JB073i010p03335

Kulak, A., Mlynarczyk, J., Ostrowski, M., Kubisz, J., & Michalec, A. (2012). Analysis of ELF electromagnetic field pulses recorded by the Hylaty station coinciding with terrestrial gamma-ray flashes. *Journal of Geophysical Research: Atmospheres*, *117*(D18). doi: 10.1029/2012JD018205

Kuak, A., & Mynarczyk, J. (2011, April). A new technique for reconstruction of the current moment waveform related to a gigantic jet from the magnetic field component recorded by an ELF station. *Radio Science*, *46*(02), 1–7. doi: 10.1029/2010RS004475

Lacroix, A., Coulouvrat, F., Marchiano, R., Farges, T., & Ripoll, J. (2019, October). Acoustical Energy of Return Strokes: A Comparison Between a Statistical Model and Measurements. *Geophysical Research Letters*, *46*(20), 11479–11489. doi: 10.1029/2019GL085369

Lacroix, A., Farges, T., Marchiano, R., & Coulouvrat, F. (2018, November). Acoustical Measurement of Natural Lightning Flashes: Reconstructions and Statistical Analysis of Energy Spectra. *Journal of Geophysical Research: Atmospheres*, *123*(21), 12,040–12,065. doi: 10.1029/2018JD028814

Levine, D. M., & Gilson, B. (1984, May). *Tortuosity of lightning return stroke channels* (Tech. Rep. No. NASA-TM-86104).

MacGorman, D. R., Few, A. A., & Teer, T. L. (1981). Layered lightning activity. *Journal of Geophysical Research*, *86*(C10), 9900. doi: 10.1029/JC086iC10p09900

Mb3a analog infrasound sensor [dataset]. (2022). Seismo Wave. Retrieved from `http://seismowave.com/home/products/infrasound-sensors/`

Mlynarczyk, J., Br, J., Kulak, A., Popek, M., & Kubisz, J. (2015). An unusual sequence of sprites followed by a secondary TLE: An analysis of ELF radio measurements and optical observations. *Journal of Geophysical Research: Space Physics*, *120*(3), 2241–2254. doi: 10.1002/2014JA020780

Novoselov, A., Dorninger, M., Diendorfer, G., Bokelmann, G., & the AlpArray Working Group. (2022, July). Seismoacoustic Study of Thunder and Lightning Using the AlpArray. *Seismological Research Letters*. doi: 10.1785/0220220064

Pasko, V. P., Inan, U. S., Bell, T. F., & Taranenko, Y. N. (1997). Sprites produced by quasi-electrostatic heating and ionization in the lower ionosphere. *Journal of Geophysical Research: Space Physics*, *102*(A3), 4529–4561. doi: 10.1029/96JA03528

Pasko, V. P., Yair, Y., & Kuo, C.-L. (2012, June). Lightning Related Transient Luminous Events at High Altitude in the Earths Atmosphere: Phenomenology, Mechanisms and Effects. *Space Science Reviews*, *168*(1), 475–516. doi: 10.1007/s11214-011-9813-9

Plooster, M. N. (1971). Numerical Model of the Return Stroke of the Lightning Discharge. *Physics of Fluids*, *14*(10), 2124. doi: 10.1063/1.1693303

Pdeboy, S. (2015). Analysis of the French lightning locating system location accuracy. In *2015 International Symposium on Lightning Protection (XIII SIPDA)* (p. 337-341). doi: 10.1109/SIPDA.2015.7339299

Quick, M. G., & Krider, E. P. (2013). Optical power and energy radiated by natural lightning. *Journal of Geophysical Research: Atmospheres*, *118*(4), 1868–1879. doi: 10.1002/jgrd.50182

Rakov, V. A., & Uman, M. A. (2003). *Lightning: Physics and Effects*. Cambridge University Press.

Ribner, H. S., & Roy, D. (1982, December). Acoustics of thunder: A quasilinear model for tortuous lightning. *The Journal of the Acoustical Society of America*, *72*(6), 1911–1925. doi: 10.1121/1.388621

Ripoll, J.-F., Zinn, J., Colestock, P. L., & Jeffery, C. A. (2014, August). On the dynamics of hot air plasmas related to lightning discharges: 2. Electrodynamics: Electrodynamics of lightning air plasmas. *Journal of Geophysical Research: Atmospheres*, *119*(15), 9218–9235. doi: 10.1002/2013JD020068

Ripoll, J.-F., Zinn, J., Jeffery, C. A., & Colestock, P. L. (2014, August). On the dynamics of hot air plasmas related to lightning discharges: 1. Gas dynamics: Air plasmas related to lightnings. *Journal of Geophysical Research: Atmospheres*, *119*(15), 9196–9217. doi: 10.1002/2013JD020067

Rison, W. (2012). *Hymex lightning mapping array*. New Mexico Tech. doi: 10.6096/MISTRALS-HYMEX.LIGHTNING.LMA

Rison, W., Thomas, R. J., Krehbiel, P. R., Hamlin, T., & Harlin, J. (1999). A GPS-based three-dimensional lightning mapping system: Initial observations in central New Mexico. *Geophysical Research Letters*, *26*(23), 3573–3576. doi: 10.1029/1999GL010856

Schulz, W. (2013). *Lightning euclid.* EUCLID. doi: 10.6096/MISTRALS-HYMEX.LIGHTNING.EUCLID

Schulz, W., Diendorfer, G., Pedeboy, S., & Poelman, D. R. (2016, March). The European lightning location system EUCLID Part 1: Performance analysis and validation. *Natural Hazards and Earth System Sciences*, *16*(2), 595–605. doi: 10.5194/nhess-16-595-2016

Soula, S., Defer, E., Fllekrug, M., van der Velde, O., Montanya, J., Bousquet, O., ... Pedeboy, S. (2015, November). Time and space correlation between sprites and their parent lightning flashes for a thunderstorm observed during the HyMeX campaign: Sprites and flash characteristics. *Journal of Geophysical Research: Atmospheres*, *120*(22), 11,552–11,574. doi: 10.1002/2015JD023894

Thomas, R. J., Krehbiel, P. R., Rison, W., Hunyady, S. J., Winn, W. P., Hamlin, T., & Harlin, J. (2004). Accuracy of the Lightning Mapping Array. *Journal of Geophysical Research: Atmospheres*, *109*(D14). doi: 10.1029/2004JD004549

Troutman, W. W. (1969). Numerical calculation of the pressure pulse from a lightning stroke. *Journal of Geophysical Research (1896-1977)*, *74*(18), 4595–4596. doi: 10.1029/JC074i018p04595

Turman, B. N. (1977). Detection of lightning superbolts. *Journal of Geophysical Research (1896-1977)*, *82*(18), 2566–2568. doi: 10.1029/JC082i018p02566

Uman, M. (1987). The lightning discharge. *Internat. Geophys. Series*, *39*, 377.

Uman, M. A., Cookson, A. H., & Moreland, J. B. (1970, June). Shock Wave from a FourMeter Spark. *Journal of Applied Physics*, *41*(7), 3148–3155. doi: 10.1063/1.1659378

Wang, J., Cao, J., Cai, L., Su, R., Zhou, M., Fan, Y., & Li, Q. (2022, September). Thunder acoustic signature for channel reconstruction in triggered lightning. *Journal of Applied Physics*, *132*(12), 123301. doi: 10.1063/5.0110866